exquisite probes for unexplored regimes of strongly interacting matter, as well as for nuclear many-body phenomena and their variations with density and isospin asymmetry.

Among the messengers probing NSs and related phenomena, gravitational waves (GWs) are unique because they are purely based on gravitational interactions, and thus travel nearly uncontaminated from the densest regions of their sources to the detectors. The potential for nuclear physics with GWs has already become evident with the spectacular first detection of a binary NS (BNS) merger, GW170817 [2]. For this event, only the inspiral epoch, when the NS and its companion are still orbiting and matter is near its ground state, was discernible in the GW data. This enabled inferring constraints on the cold equation of state (EOS) above nuclear density from measurements of the NS's tidal deformability, a characteristic parameter that depends on the properties of matter and — together with the electromagnetic counterpart — provided the first definite identification of the central engine of a kilonova and the association of a BNS merger with a GRB. Since then, at least four more events likely involving one or two NSs in a binary were discovered, but apart from the masses of the coalescing objects, no new information relevant for nuclear physics could be extracted [1475, 2600, 2601].

Current detectors are mainly sensitive to the inspiral of NS binary coalescences. The outcomes beyond that vary depending on the type of binary system and its parameters. For mergers of NSs with a black hole (BH), the NS either becomes tidally disrupted, which leads to a strong suppression of the GW signal, or plunges into the BH, or is partially disrupted. In all such scenarios, the final remnant is a BH, and cases with tidal disruption are accompanied by electromagnetic counterparts. The mergers of two NSs have different outcomes depending on the initial systems: prompt collapse to a BH or the formation of a rotating massive NS heated by shocks during the merger process, which either collapses to a BH after shedding enough angular momentum or forms a stable NS remnant. In the latter two cases, the post-merger behavior is highly dynamical, involving differential rotation, oscillations, and dissipation, along with various microphysical processes, small-scale magnetohydrodynamic instabilities, and higher temperatures. This aftermath of a BNS merger provides a window onto a completely unexplored swath of the parameter space of subatomic physics that represents a complex nonperturbative regime in-between our current understanding of matter at low baryon densities from nuclear physics and heavy-ion collisions, and the regime of unreachable high densities where first principle calculations within quantum chromondynamics (QCD), the theory of the strong interaction, are valid.

The coalescences of NS binaries are also among the key production sites of elements heavier than iron in the cosmos. Heavy elements can be synthesized from the neutron-rich material expelled during BNS mergers or the tidal disruption of NSs by BHs and winds from the remnant accretion disks. The subsequent radioactive decay of these elements powers a kilonova electromagnetic transient.

In addition to binary mergers, future multi-messenger observations include the possible discoveries of signals from (i) a nearby (galactic) core-collapse supernova (CCSN), where the GWs and neutrinos contain imprints of the yet poorly understood explosion mechanism, dense matter properties in regimes complementary to heavy-ion collisions and BNS mergers, and the possible hot proto-NS, and (ii) rotating isolated NSs with a deformation (e.g. elastically- or magnetically-induced mountains on their surface or unstable oscillation modes) encoding

JCAP03(2026)081

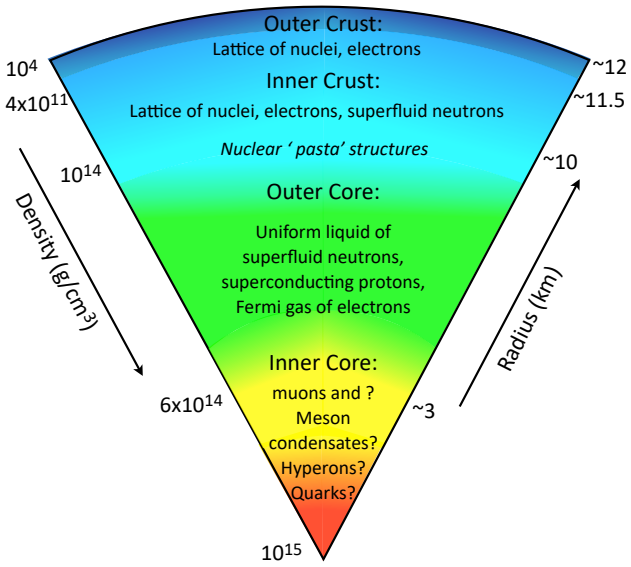

Figure 119. Conjectured structure of a cold, mature neutron star. In the interior, matter ranges over nearly an order of magnitude in density and encompasses a variety of different phases and physical properties. Reproduced from [15].

information about the structure of the crust and the behavior of dense matter under the influence of a strong magnetic field.

Due to the projected increase in sensitivity of the existing detector network of the LIGO, Virgo, and KAGRA (LVK) facilities in the coming years, and based on the event rates inferred from the past detections, we expect GW measurements of potentially dozens of binary merger events involving NSs in the coming years [7, 392]. This will represent a larger sample of the diverse population of NSs, with the nearby events measured with higher accuracy and possible access to the tidal deformability characterizing the dominant EOS signatures in GW signals. Several cases with electromagnetic counterparts are also expected [2187, 2602–2605]. Further upgrades, A# [2436] and VirgoNext, are planned to fill the gap between the LVK run O5 and the onset of next-generation observatories projected for the late 2030's [2606]. These detections will already enable significant advances in our understanding of dense matter in NSs.

However, even after these planned upgrades, the capabilities of the current detectors will remain limited in sensitivity and bandwidth, especially at the high frequencies corresponding to the signals of the post-merger phase. Next-generation observatories such as ET will have a significantly higher sensitivity, e.g., GW170817 would have a signal-to-noise ratio of up to fifty times larger than current detectors due to the higher sensitivity and the larger frequency range that ET will cover. Moreover, ET is expected to detect several tens of thousands of BNS merger events per year [15, 16] and thus probe the diverse population of NSs. Its increased low frequency sensitivity is important for sending early-warning alerts to electromagnetic telescopes before the BNS mergers and for higher precision measurements during the inspiral phase. The increased high frequency sensitivity will enable higher precision measurements of matter effects in the late inspiral and tracing the details of the behavior of matter during the

JCAP03(2026)081

merger and its aftermath. For inspirals, this will not only enable precision measurements of tidal deformability along with the NS masses and spins, but also give access to subdominant effects, such as the tidal excitations of characteristic NS modes, among others, which will provide further details about NS matter. The dominant GW observables from the post-merger regime are the frequency associated with the rotation of the dynamical remnant and its lifetime, with the frequency spectrum also involving a number of additional features related to various microphysics properties. For NS-BH binaries with tidal disruption, the disruption frequency provides additional information on the cold EOS. The possibility of performing a GW observation from a CCSN event and the subsequent proto-NS (PNS) evolution, as well as of detecting GWs from isolated NSs also significantly increases with ET. Measurements with ET are thus poised to yield profoundly transformative advances for nuclear physics. Accompanying electromagnetic and neutrino signals to the mergers will yield complementary information and, when combined, provide copious insights into a variety of microphysics of dense matter and the production of heavy elements. Conversely, with adequate nuclear theory support, NS binaries observed with ET can be used to test the theory of gravity and its matter couplings in the largest density and pressure regimes available in nature and probe for dark matter, as detailed in section 2.

This section is organized as follows. In section 7.2 we recapitulate the current status of our knowledge on the properties of dense and hot matter in NS-related environments. In section 7.3 we discuss the potential of GW detections with ET to impact our understanding of subatomic physics. The inspiral phase of a BNS merger, the tidal disruption of NSs in NS-BH systems, and the GWs from an isolated NS thereby probe essentially cold matter, whereas in the BNS post-merger phase and during a CCSN event or within a PNS, matter is hot. Section 7.4 is devoted to a discussion of the different uncertainties in the theoretical modeling that underpins the interpretation of the data for nuclear physics and will be the main limiting factor for the science returns from measurements with ET. We also discuss degeneracies with other physical effects, such as those due to modified gravity or to dark matter, in the interpretation of the detected signal for subatomic physics. We conclude in section 7.5 with a summary of the key takeaway points and synergies with other facilities.

7.2 Current status of microphysics properties

To motivate the science potential of ET, we first review the current status of our knowledge and remaining open questions for the properties of dense and hot matter, which also enter the modeling of the various astrophysical systems considered in this section. This includes the EOS discussed in section 7.2.1, as well as the different reactions rates from out-of-equilibrium processes which cannot be included in the EOS, and are discussed in section 7.2.3.

7.2.1 Equation of state modeling

The structure of cold, mature NSs can be described by a one-parameter EOS that relates the pressure to the energy density, as the temperature is well below the Fermi temperature and weak (β-)equilibrium has been reached. The typical density range extends from values encountered on Earth up to several times the nuclear saturation density, $n_{\rm sat} \approx 0.16$ fm^{-3}, which corresponds to $\rho_0 \approx 2 \times 10^{14}$g/cm^3. In addition, the study of related astrophysical

JCAP03(2026)081

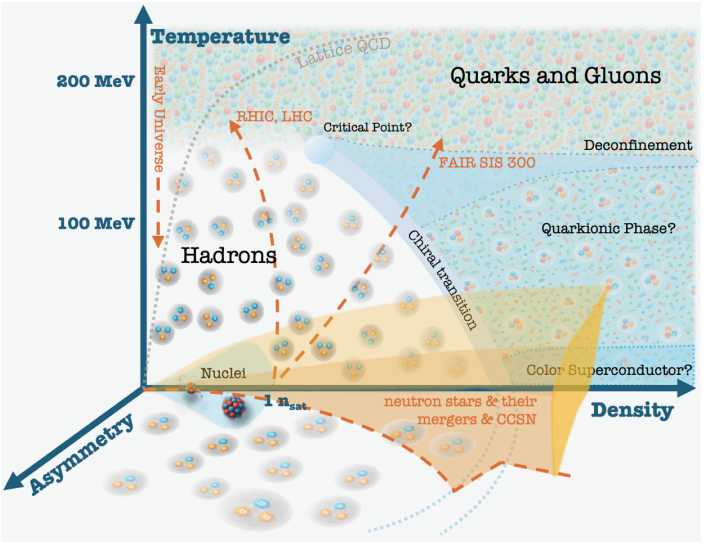

Figure 120. Depending on the thermodynamic conditions, matter can exist in different forms, like nuclei, gas of nuclear clusters, gas of hadrons, and strongly-coupled quark-gluon plasma states. The temperature-density-isospin asymmetry diagram illustrates the different thermodynamic conditions spanned in NSs, BNS mergers, CCSN, PNSs, as well as in nuclei and the early universe. The regimes that can be explored in different terrestrial facilities are also indicated. Reproduced from [2607]. CC BY 4.0.

phenomena, e.g., the post-merger phase of a BNS merger, CCSN, PNSs and the formation of stellar BHs, requires EOSs, dubbed general purpose EOSs, that also include a wide range of temperatures $0 \lesssim T \leq 150$ MeV and charge fractions $0 \leq Y_Q \leq 0.6$, where $Y_Q = n_Q/n_B$ with n_Q defined as the electric charge density in hadrons and n_B the baryon number density. By electric charge neutrality, Y_Q equals the fraction of charged leptons, i.e., electrons and muons, which appear in the higher density regions of NSs. The regimes of baryon density, temperature, and isospin parameter space covered by NSs are illustrated in the phase diagram in figure 120. Describing the different properties of matter over this vast range of thermodynamic parameters is a challenge. Firstly, over these large ranges of density scales, matter characteristics change dramatically, from a mixture of different nuclei to uniform strongly interacting matter, containing, in the simplest case, just nucleons but potentially more exotic components such as hyperons or mesons. Moreover, a transition to deconfined quark matter might occur at high densities. Secondly, the extreme densities and asymmetries involved in NSs are inaccessible to both terrestrial experiments and, so far, theoretical first-principles calculations, which are hindered by the non-perturbative character of this strongly interacting many-body system.

7.2.1.1 NS EOS. Over the last decades, numerous models for the NS EOS have been developed. In what follows, we review some of the main classes of models, and expose the change of paradigm caused by large computing resources and availability of new astrophysical data, advantages and disadvantages of different strategies, and the potential onset of non-nucleonic degrees of freedom.

JCAP03(2026)081

Agnostic EOS models. Agnostic EOS models can either be non-parametric, e.g., based on Gaussian processes, or parametric, e.g., based on a piece-wise polytropic or spectral representation, or a parametrization of the speed of sound. The parameters of such a representation can be constrained based on a number of considerations that often include causality and thermodynamic stability, but also astrophysical measurements and ab initio calculations of pure neutron matter; see, e.g., refs. [2483, 2608–2611] and references therein. Some models also include constraints on the high density part of the EOS based on requiring compatibility between the behavior of the EOS at densities $n \lesssim 5n_{\rm sat}$ and in the quark phase at ultrahigh densities of $n \sim 40n_{\rm sat}$ accessible to perturbative QCD calculations, see, e.g., refs. [2612–2614].

Agnostic models enable exploring the relation between properties of the EOS and global NS properties. The latter include mass, radius, compactness, moment of inertia, tidal deformability, and Kepler frequency.[60] While flexible, computationally cheap, and straightforward to use, these models lack a connection with the underlying microphysics. Hence, no information on the interactions and composition of the matter is available, and compliance with known properties of nuclear matter has not always been checked.

Semi-agnostic models. Semi-agnostic models have been designed to account for basic knowledge of nuclear matter while still allowing for significant flexibility. Some of these models rely on a meta-modeling approach, i.e., a flexible model where the parameters can be tuned to reproduce present information from nuclear physics and/or constraints from astrophysics. For instance, a useful basis [2615–2618] is a Taylor expansion of the energy per particle in terms of particle number density of neutrons and protons $n = n_n + n_p$ and the isospin asymmetry $\delta = (n_n - n_p)/n$ (see refs. [2619, 2620] for a discussion)

$$\begin{aligned}\frac{E(n,\delta)}{A} &= E_{\rm sat} + \frac{1}{2!}K_{\rm sat}x^2 + \frac{1}{3!}Q_{\rm sat}x^3 + \dots \\ &\quad + \left[E_{\rm sym} + L_{\rm sym}x + \frac{1}{2!}K_{\rm sym}x^2 + \frac{1}{3!}Q_{\rm sym}x^3 + \dots\right]\delta^2 \ + \dots,\end{aligned} \tag{7.1}$$

with $x = (n - n_{\rm sat})/(3n_{\rm sat})$ denoting the deviation from saturation. This enables directly incorporating constraints on the coefficients of the expansion, that is, the empirical nuclear matter parameters such as the energy per particle at saturation $E_{\rm sat}$, the nuclear compressibility $K_{\rm sat}$, the symmetry energy $E_{\rm sym}$, the slope $L_{\rm sym}$ and curvature $K_{\rm sym}$ of the symmetry energy; for a relativistic version see [2621]. While low-order parameters, up to $K_{\rm sat}$ ($L_{\rm sym}$) for the isoscalar (isovector) channel are relatively well constrained by ab initio nuclear theory and low-energy nuclear experiments, large uncertainties still affect higher order parameters. Other models employ a chiral effective field theory (χEFT)-inspired expansion in terms of the neutron and proton Fermi momenta [2622]. The increased flexibility of these models makes them suitable for Bayesian inferences. The related meta-model approach, which is based on an empirical parameterization inspired by eq. (7.1), enables predicting observables with uncertainties controlled by our present theoretical and experimental knowledge of nuclear and NS physics.

[60] The Kepler frequency is the maximum possible frequency of a rigidly rotating star.

JCAP03(2026)081

Phenomenological models. Phenomenological models employ effective interactions to describe the properties of atomic nuclei. The forms of the interactions are motivated by ab initio theory while the values of parameters are adjusted by extensive fits to different data from nuclear structure, particle production and flow in heavy-ion collisions, microscopic calculations of neutron matter and, most recently, multi-messenger observations of NSs. The non-relativistic models use the Hartree-Fock technique to solve for the nucleonic equations of motion based on a Hamiltonian. Most models of NS EOS rely on the zero-range Skyrme interaction [2623] while others employ momentum dependent Gogny interactions [2624]. For densities above a few times n_{sat}, a number of deficiencies have been identified, for instance, superluminal sound speeds and Fermi velocities [2625] or negative symmetry energies. These make the extrapolation to arbitrarily high densities questionable unless these deficiencies are fixed. The relativistic models, also known as covariant density functional models, are based on relativistic Lagrangian densities. Most models of NS EOS correspond to the Hartree approximation and are finite-range [2626]. Relativistic Hartree-Fock models exist as well [2627]; the Fock term is responsible for a strong density increase of the symmetry energy, which leads to large proton fractions in the core and low threshold densities for the onset of direct Urca processes, responsible for fast NS cooling. The ensemble of these models is evocative for how the limited information on nucleon-nucleon effective interactions away from saturation and isospin symmetry gets translated into large uncertainties in dense and/or isospin asymmetric matter [2628]. Use of both non-relativistic and relativistic phenomenological models in Bayesian inferences of dense matter EOS and composition [2629–2632] helps identify correlations between nuclear matter parameters and NS properties and test their robustness with respect to the energy density functional. The Induced Surface Tension model, a multicomponent parametric model for the EOS [2633, 2634] enters this category, too. An advantage of phenomenological models is their physical underpinning and the possibility to apply the constrained effective interactions to other physical environments, such as nuclear structure calculations. Extensions to finite temperature are straightforward. Extensions to incorporate non-nucleonic degrees of freedom (d.o.f.) have also been developed.

Ab-initio models. Ab-initio models represent a theoretical approach in which the EOS is derived by solving the complicated nuclear many-body problem [2635] starting from few-body interactions. For the nucleon-nucleon case, very high precision interactions exist from meson-exchange [2636–2639] and potential models [2640, 2641], or, more recently, from χEFT [2642–2644]. The latter has the additional advantage that three-body forces can be constructed in a consistent manner rather than adding them purely phenomenologically. For other particles, such as hyperon-nucleon interactions, the situation is much less favorable, in particular due to the scarcity of experimental data. The most commonly used microscopic many-body approaches include the (Dirac)-Brueckner-Bethe-Goldstone theories [2635], the self-consistent Green's function technique [2645, 2646], the variational method [2647], the correlated basis function formalism [2648], Quantum Monte Carlo techniques [2649, 2650], ladder resummations that reorganize scattering data without resorting to assumptions on microscopic dynamics [2651], and the use of renormalisation group improved interactions [2652] or many-body perturbation theory (see e.g. ref. [2653]). Details of these approaches are reviewed in [2654, 2655].

JCAP03(2026)081

Non-nucleonic degrees of freedom. An interesting feature at high densities is the potential appearance of new d.o.f. Generic arguments based on the energetics suggest that extra baryonic d.o.f., e.g., Λ, $\Sigma^{-,0,+}$ and $\Xi^{-,0}$ hyperons or $\Delta^{-,0,+,++}$ resonances can be populated in dense matter [2656]. High densities can also favor the appearance of mesons, e.g., kaons and pions, as well as meson condensates [2656]. This includes inhomogeneous condensates [2657] which entail an anisotropy and require a description of the stress-energy tensor $T^{\mu\nu}$ beyond a simple perfect-fluid EOS, as further discussed in the paragraph on nonhomogeneous energy-momentum tensors below. Generally, the onset of any extra d.o.f. entails a softening of the EOS, that is a reduction of the pressure, and consequently a reduced NS maximum mass. A wealth of studies nevertheless testify that the appearance of any of the above-mentioned particles is compatible with the current observational lower bounds on the NS maximum mass. The vast majority of models with these "exotic" d.o.f. currently available rely on covariant energy density functional models, see e.g. [2658–2663]. The parameters governing the interactions of the non-nucleonic d.o.f. are, however, very poorly constrained. Rare measured properties of hypernuclei set some constraints on the hyperonic interactions [2664, 2665] (more are expected from femtoscopy studies of baryon-baryon correlations in heavy-ion collisions) and many models apply symmetry arguments from an underlying simple quark model to relate the different coupling parameters and thus reduce the parameter space, see e.g. [2666, 2667]. Under certain conditions, the onset of these d.o.f. can occur via a density-driven phase transition [2658, 2663].

Another possibility for matter above a few times $n_{\rm sat}$ is that deconfined quark matter phases emerge. Hybrid compact stars, i.e., stars with a quark core surrounded by a nuclear envelope containing a minimal liquid inner shell and a solid crust, represent an interesting subclass of compact stars where a phase transition to quark matter is assumed to take place. The fundamental theory of the strong interactions, QCD, predicts an asymptotically-high density phase of color superconductivity, which shares features with a perturbative-QCD gas but in which color and flavor symmetries are partially broken, locked into a remaining subgroup "CFL" phase [2668, 2669]. This provides insights into the EOS of strongly interacting matter at presumably unreachably high densities. At lower densities, additional phases such as the 2SC in which only two quark flavours (u,d) participate in the condensate may exist. However, the theory cannot currently be employed in the low-temperature, finite density and neutron-proton asymmetry regime typically encountered in cold NSs. Therefore, in most cases, effective models such as the Nambu-Jona-Lasinio model, the MIT bag model, or a constant sound-speed parametrization are often used to model quark phases in hybrid stars, see, e.g. refs. [2670, 2671], and ref. [2672] for a review. An alternative possibility for the state of quark matter in NSs is that a quarkyonic phase emerges, where a Fermi sea of quarks defines the matter and confining forces are only realized at the surface. Such a model can allow quarks to exist at rather low densities [2673, 2674] and interestingly does not necessarily lead to smaller radii for hybrid stars compared with purely hadronic ones [2675]. An even more radical possibility is that strange quark matter is absolutely stable [625]. In that case compact stellar objects entirely made of strange quark matter can exist and have large masses and radii, while stars made of nucleons, hyperons and resonances can also exist and have small radii but not too large masses [2324, 2665]. Due to the phenomenological

JCAP03(2026)081

nature and the impossibility to explore dense quark matter in terrestrial experiments, the parameters of the different models are difficult to determine, or to relate to one another and to QCD. However, these models allow testing the consequences of a hadron to quark phase transition on the NS's structure, cooling, oscillation modes, etc. Moreover, there have been recent advances on informing the NS EOS using holographic approaches for describing strongly-interacting QCD matter at high baryon density [2676–2680], or with functional renormalisation group techniques [2681–2683].

Crust models. Thus far, we discussed models for matter at high density, which is the most relevant for describing the NS core. At lower densities, nuclear clusters are formed under screened electromagnetic or frustrated nuclear interactions and arrange in crystalline structures. The properties of the crust are important, for instance, for (accreting) NS cooling [2684], for magnetic, thermal and rotational evolution of pulsars [2685], NS ellipticity that can be potentially measured by GW observations [2686], and for explaining pulsar glitches [2687]. In these regimes, i.e. at low density and relatively low temperatures (though this also holds at slightly higher temperatures for the so-called general-purpose EOSs, see section 7.2.1.2), different approaches are employed to compute the EOS and the composition, either (i) using the so-called single-nucleus (SNA) or one-component plasma (OCP) approximation, where the composition of matter is assumed to be made of one representative heavy nucleus (the one that is energetically favored), and possibly unbound nucleons, or (ii) considering the distribution of an ensemble of nuclei at finite temperature or using a multi-component plasma approach (often called nuclear statistical equilibrium, NSE, in the context of general purpose EOS). While the internal constitution of the outermost layers of a non-accreted, cold NS crust is completely determined by atomic masses that are either experimentally measured or predicted by theoretical mass tables, the description of the inner crust, where unbound nucleons are also present, relies on theoretical models. Methods to calculate the NS crust usually treat nucleons as non-uniformly distributed within a cell of a given shape and size, either considering them as localized particles, or assuming a nucleon density distribution, in a charge neutralizing electron background. Despite remarkable progress in the development of many-body methods, ab initio calculations of the crust are still unattainable, thus phenomenological models are employed. Most of the crust calculations rely on the Wigner-Seitz cell approximation, and while a spherical cell is usually assumed at lower density, since nuclear clusters are (quasi-)spherical, at higher densities in the inner crust, other geometries have been considered that take into account the possible appearance of non-spherical structures collectively known as 'pasta phases' [2688]. Within this picture, different methods have been used in the literature to model the inhomogeneous crust. Fully quantum mechanical approaches that incorporate shell and pairing effects, which are important in determining the ground-state composition of the crust, include Hartree-Fock, Hartree-Fock+BCS, and Hartree-Fock-Bogoliubov approaches (see e.g. the pioneering calculations of ref. [2689], and the more recent works [2690–2692]). These calculations are however computationally expensive. For this reason, many studies have employed compressible liquid-drop models (e.g. refs. [2688, 2693, 2694] and the more recent ones of refs. [2695–2702]), that parameterize the energy of the system in terms of individual contributions, such as bulk, surface, and Coulomb energy; nucleons inside the neutron-proton clusters and free nucleons outside are assumed to be uniformly distributed

JCAP03(2026)081

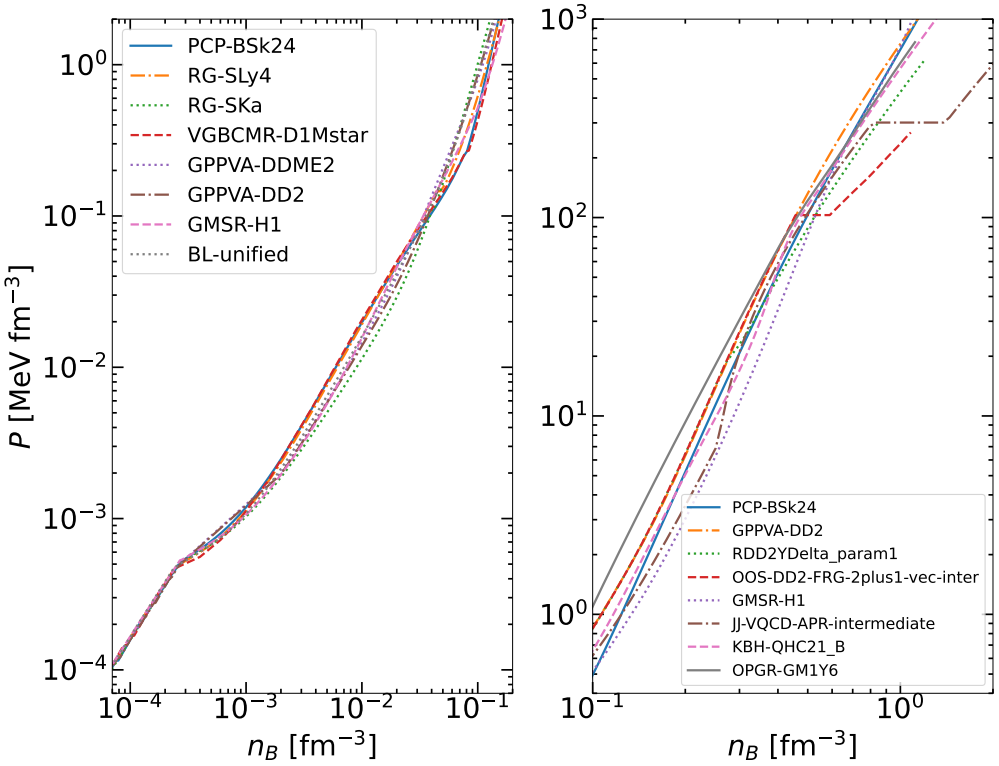

Figure 121. Pressure versus baryon number density for different EOS models taken from the CompOSE database [2716]. *Left panel:* different unified nucleonic EOSs in the crust-core density regime (changes of slope indicate the transition from the outer to the inner crust and from the crust to the core). *Right panel:* different EOS models (nucleonic, with admixtures of hyperons and Δs, and with a phase transition to quark matter) in the high-density regime in the core.

and treated separately. A more realistic effective treatment involves the use of semi-classical methods such as the (extended) Thomas-Fermi model, that determines the density distribution of nucleons in the cell using a given energy density functional, thus allowing for a consistent modeling of nucleons 'inside' and 'outside' clusters (see e.g. refs. [2696, 2703, 2704] for recent works); although shell effects which play a role for the composition for the inner crust are usually lost, they can be restored perturbatively (see e.g. the recent works of refs. [2705–2707] and references therein). Alternative approaches such as time-dependent Hartree-Fock methods based on a wavelet representation (e.g. [2708]), classical molecular dynamics (e.g. [2684, 2709, 2710]), or quantum molecular dynamics (e.g. [2711–2713]), have also been employed, see e.g. refs. [2619, 2654, 2672, 2714, 2715] for a review.

We note that ensuring consistency between the description of the NS core and crust is important for EOS models, as has been thoroughly discussed in e.g. [2628]. Most approaches to construct full NS EOSs have relied on an ad-hoc matching of three EOSs, corresponding to the outer and inner crusts and the core, computed using different models. Often, arbitrary values have been employed for the various transition densities. The rationale behind this procedure is that NS mass and radius are determined mainly by the core EOS. However, the crust-core matching procedures still alters the predicted values of NS tidal deformability and radius by a few to ten percent [2628, 2717, 2718]. Although these uncertainties seem

JCAP03(2026)081

relatively small compared with the current precision of observational data, they will become particularly relevant for next-generation GW observatories such as ET. In order to minimize these uncertainties, the matching must be smooth, causal and thermodynamically consistent. To avoid any arbitrariness in the matching procedure, so-called unified EOSs, where the same nuclear model is employed for the different regions of the NSs, must be used. Providing such unified EOS models has been the focus of much recent effort by the nuclear physics community, see e.g. refs. [2695, 2697, 2703, 2705, 2719–2721] and the CompOSE database [2716, 2722] for a collection. The CUTER tool [2723] enables constructing a consistent crust from a given core EOS.

Figure 121 shows examples of a collection of beta-equilibrated cold NS EOSs from the CompOSE database: the left panel shows unified nucleonic EOSs (changes of slope indicate the transition between the outer and the inner crust, and between the crust and the core) in the crust-core density regime, while the right panel illustrates different EOSs (some of which include heavy baryons or a phase transition to quark matter) in the core. The largest uncertainties are indeed observed in the high-density regime in the NS core.

Nonhomogeneous energy-momentum tensors. It is customary to approximate the energy-momentum tensor of NS matter by that of a perfect fluid in thermodynamic equilibrium, $T^{\alpha\beta} = (\epsilon+P)u^\alpha u^\beta + P g^{\alpha\beta}$ with a local fluid velocity u satisfying $u^2 = -1$ (in geometric units), energy density ϵ and pressure P. Later on we will discuss dissipative effects, for example in subsection 7.2.3, which can be implemented by adding a non-ideal fluid piece τ_{ij} to the energy-momentum tensor. Further, anisotropies in NS matter can develop which require a non-rotationally invariant form for the tensor, affecting the formulation of the Einstein equations. This can happen for various reasons [2724]. One is the presence of external privileged directions such as magnetic fields [2725–2727], see 7.3.1.2 below, or rotation vortices which affect matter at smaller scales. But matter can also organize itself in crystalline structures to relax the electrostatic energy (Coulomb interactions in the crust) or to alleviate the pressure (because neutrons exclude a finite volume due to the repulsive $n-n$ short-range potential, arranging them in compact packings can relax the free energy) [2728] and this entails a breaking of rotational invariance. Anisotropies can also arise when two phases coexist [2729]. Likewise, if quark phases emerge in NSs, it is possible that inhomogeneous chiral condensates may form, although this is still under active theoretical investigation [2730].Thus, it is interesting to explore the capabilities of detectors such as ET to probe for anisotropic stress-energy tensors, which would have important implications for understanding the microscopic physics of NSs.

7.2.1.2 General purpose EOS. Matter in CCSN, PNSs, or the post-merger phase of a BNS coalescence, is heated and not necessarily in β-equilibrium. Therefore, thermal and compositional effects have to be incorporated in the EOS. Matter is assumed to consist of hadrons or, alternatively, deconfined quarks, leptons and photons and taken to be in thermal equilibrium for hadrons, photons and charged leptons, as well as chemical equilibrium with respect to the strong interaction. Commonly, the corresponding EOSs, called "general purpose", are provided as functions of temperature T, baryon number density n, and the charge fraction Y_Q (if electrons are the only considered charged leptons and charge neutrality

JCAP03(2026)081

holds, $Y_Q = Y_e$; if muons are included, then $Y_Q = Y_e + Y_\mu$, with Y_μ the muon fraction); see e.g. ref. [2716].

Charged leptons and photons are in general simply considered as ideal gases and the discussion below therefore focuses on the contribution of strongly interacting matter, hadrons and/or quarks. Due to the computational efforts needed to cover the entire range of thermodynamic parameters and the different matter compositions from a gas of (interacting) nuclei to potentially a color-flavor locked condensate phase, most of the existing general purpose EOS employ phenomenological models for the interactions with a few exceptions. EOSs with various particle blends have been built. Many of these general purpose EOSs are available for public use on CompOSE [2716, 2722]. Information on thermodynamic properties and optionally on particle composition and microscopic quantities such as interaction potentials is provided in tabular form with a mesh fine enough to allow usage in numerical astrophysical simulations or data interpolation.

In the absence of constraints from nuclear experiments, insights into the thermal behavior of matter can only be gained by confronting the predictions of available models against each other and by comparing with ab initio calculations. Such comparisons reveal that — at least for purely nucleonic models — the effective mass and its density derivative entering the statistical partition function play the dominant role in the thermal corrections to thermodynamic state variables [2731–2733]. However, due to the different ways the effective mass depends on the underlying interaction within the different types of models, large qualitative differences exist between the predictions (e.g. [2734]), and it is difficult to attribute a generic thermal behavior to the EOS.

Non-nucleonic degrees of freedom can also be thermally excited and are generally found to increase in abundances with temperature, see e.g. [2662, 2735–2740]. The thermodynamic properties are very sensitive to the number of particle d.o.f. and less sensitive to the details of the underlying interaction [2741]. A potential phase transition from hadronic to quark matter along with the technical solution adopted to build the phase coexistence impacts all thermodynamic state variables, too, see [2741] and references therein. In particular, a phase coexistence built according to the Maxwell construction, where the pressure in the mixed phase remains constant, leads to vanishing values for the speed of sound, while a Gibbs construction leads to a smooth density dependence in most cases.

Approximate methods for extending cold EOSs to finite temperatures exist as well, with flexibility and low computational cost being their most important assets. The most commonly used example is the Γ-law [2742], which consists of supplementing the cold EOS with an ideal-gas-like contribution. As such, any density-, temperature-, composition- and interaction-dependence is disregarded, which represents a serious drawback. An improved solution is provided by attempts which use the finding that the effective mass dominates thermal effects in the EOS, see for instance [2743, 2744]. The analytical expressions proposed in [2744] are able to reproduce the thermal pressure of a given class of models to within a few percent. However, as stated above, it cannot cover the model dependence and thus uncertainties in thermal effects.

JCAP03(2026)081

7.2.2 Current constraints on EOS and matter composition

At present, the different approaches to the NS EOS yield generally similar results up to about twice the saturation density and significantly diverge at larger density [2655]. The main source of uncertainty is the extrapolation of the nucleonic interaction to large density. In fact, nuclear data from both experiments and theoretical ab initio calculations provide information only up to less than two $n_{\rm sat}$. For the phenomenological EOS models, their spread at high density can be related to the use of parameters whose values are fitted on experimental data that is approximately available for symmetric matter around saturation density; for the ab-initio approaches, it is due to the different high-density behavior of nucleonic three-body forces, which are mainly constructed at saturation density and then extrapolated. NS matter is also poorly constrained due to it being neutron rich, i.e. very isospin asymmetric. Apart from first-principle constraints including causality, current constrains on the EOS come from nuclear physics (mainly from nuclear structure data, heavy-ion collision experiments, and theoretical ab initio calculations of pure neutron matter) and from astrophysical observations.

The theoretical ab initio calculations of pure neutron matter are particularly interesting since they impose constraints on the symmetry energy, i.e. the behavior of the EOS upon passing from symmetric nuclear matter to more neutron rich matter as in NSs. They have been implemented in several approaches to the EOS, see e.g. [2609, 2613, 2745, 2746], but again the range of validity is limited to below $2n_{\rm sat}$. At higher density, much progress has recently been achieved on completing higher-loop calculations in perturbative QCD to describe matter at densities $\gtrsim 40n_{\rm sat}$, see e.g. refs. [2747, 2748]. As discussed in refs. [2614, 2749], improving the theoretical knowledge in such high-density regimes well beyond what is encountered in NSs can have implications for NS EOS models.

Laboratory experiments also give information up to or slightly above saturation density, and especially for isospin-symmetric matter (see e.g. refs. [2619, 2654, 2655] for a review). Note that the recent PREX-II (CREX) measurement of neutron skins in ^{208}Pb (^{48}Ca) (see ref. [2750] and refs. therein) is sensitive to the symmetry energy, too; see, however, e.g. refs. [2611, 2751] for a critical discussion of the interpretation for parameters in eq. (7.1) in view of other constraints. (Semi-)agnostic approaches, too, show the impact of the lack of data beyond that range in density and for asymmetric matter. As discussed previously, the situation is even more complicated for hot and dense matter, since currently there are no experimental or observational data in the relevant parameter regimes, and only benchmark ab initio calculations can provide some theoretical information.

Astrophysical observations have led to constraints on the NS EOS in various ways. For example, information on the EOS comes from NSs with high masses $\gtrsim 2M_\odot$ [1810, 1817, 1818, 2752, 2753], which sets a lower limit on the maximum mass the EOS needs to support, joint estimates of NS mass and radius by NICER [2754–2757], and tidal deformability measurements from GW170817 [2, 4]. To be more precise on the latter, during the inspiral of coalescing BNSs, the dominant EOS-dependent effects in the emitted GWs is characterized by the tidal deformability parameter Λ that quantifies how easily one object in a binary system is deformed due to the gravitational field of the companion; see [2758] and references therein for a review. Considering a static quadrupolar tidal field $\mathcal{E}_{ij} = C_{0i0j}$ in the rest frame of the NS, with C_{0i0j} the time-space components of the Weyl curvature tensor due to the

JCAP03(2026)081

companion, the induced quadrupole moment Q_{ij} characterizing the quadrupolar deviation of the NS exterior spacetime away from spherical symmetry at large distances, is given to linear order by [293, 294, 2759, 2760]

$$Q_{ij} = -\lambda_2 \mathcal{E}_{ij} \ . \tag{7.2}$$

The tidal deformability λ_2 is expressed in terms of the $l = 2$ tidal Love number k_2 (in units $c = G = 1$) as[61]

$$\lambda_2 = \frac{2}{3} k_2 R^5 \, , \tag{7.3}$$

with R the star radius, and k_2 has typical values of order 0.1 but strongly depends on the NS mass and EOS [2758]. A related quantity is the dimensionless tidal deformability defined as

$$\Lambda \equiv \frac{\lambda_2}{M^5} = \frac{2}{3} k_2 \frac{R^5}{M^5} = \frac{2}{3} k_2 C^5, \tag{7.4}$$

where M is the mass of the star and $C \equiv M/R$ is its compactness. Although λ_2 and k_2 are the most commonly considered tidal parameters in the context of NS binary systems, they are only the first in a series of tidal parameters of different types and orders that arise from the study of generic static tidal perturbations. However, higher multipolar contributions of λ beyond the quadrupole λ_2 (e.g. the octupolar λ_3 or hexadecupolar λ_4 contributions) are much smaller. Their values are computed by solving the Einstein field equations coupled with the matter equations of motion for linear, static perturbations around an equilibrium configuration. Current models used for measurements also include effects of spin-induced multipole moments, which contribute GW imprints from EOS-dependent rotational Love numbers [2762]. In addition, effects of dynamical tides due to the fundamental modes of the NS introduce a further dependence of the GW signal on the EOS-dependent fundamental mode frequency. Current data are not sensitive to all these parameters, and thus in the data analysis for GW170817 they were eliminated in favor of Λ by using quasi-universal relations. At this point, it is worth highlighting that although EOS-independent relations between NS macroscopic parameters have often been employed when interpreting GW data, e.g., [2460]. For next-generation observatories, the use of quasi-universal relations in parameter extraction leads to larger uncertainties on the extracted parameter than direct EOS inference [2763, 2764].

A variety of EOS models from the different categories discussed in section 7.2.1 have been employed with different levels of input from nuclear experiments and theory to study the impact of the measurement of Λ from the event GW170817 (see e.g. ref. [2758] for a review) and other astrophysical data on the NS EOS, the composition of dense matter, empirical nuclear matter parameters or parameters of a particular model. The availability of large computing resources have thereby motivated numerous statistical analyses to infer the information employing different techniques, such as Bayesian analyses or machine learning, focusing on a particular measurement or combining different ones, see e.g. [2612, 2617, 2622, 2630, 2631, 2756, 2757, 2765–2770].

[61] In the Newtonian limit the perturbing tidal field $\mathcal{E}_{ij}$ is defined as the second spatial derivative of the external field, resulting in units of inverse length squared [2761] whereas the quadrupole moment has units of length cubed.

JCAP03(2026)081

The main results can be summarized as follows:

(i) The progressive incorporation of different observations narrows down the cold EOS, but current constraints remain loose and are insufficient to discriminate between models or to determine the composition of high density (and hot) matter. Indeed, the relation between EOS and composition is not free from ambiguity, and very similar EOSs (thus almost indistinguishable mass-radius or mass-Λ relations) can be obtained under different hypotheses on the underlying microphysics, giving rise to the so-called "masquerade" effect [2672]. We also note that even a very precise knowledge of the NS EOS does not pin down the matter composition without any additional information, such as accurate measurements on the symmetry energy at high density or possibly complementary information from dynamical NS observables [1231, 2771]. The composition and in particular a change with respect to a purely nucleonic one considerably affects transport properties and thus NS cooling [2772] as well as the evolution of oscillation frequencies [2773], but no conclusive measurements exist today, although the recent discovery of three young and cold objects might be interesting in this respect [2774];

(ii) In addition to the reduced maximum mass, the onset of new d.o.f. in general leads to a sizable reduction of radii and tidal deformabilities for intermediate mass NSs, too. Current constraints can accommodate the presence of additional particles, such as Δ isobars (e.g. [2775, 2776]) or hyperons [2662, 2777–2780]. The semi-agnostic modeling of a nucleonic EOS has also been used as a null hypothesis to search for exotic d.o.f., indicating a mild tension between the GW data and ab-initio nuclear physics calculations [2781], however, the statistical significance of the discrepancies is currently insufficient to be conclusive. Overall, current astrophysical data are not constraining enough and remain compatible as well with non-nucleonic as with purely nucleonic EOSs [2620, 2622, 2746, 2768];

(iii) If the non-nucleonic particles appear via a first-order phase transition, with a density jump at constant pressure, the global properties of compact stars may differ significantly from the nucleonic counterparts. In particular, NSs with the same mass but different compactness dubbed "twin stars" can appear in the mass-radius diagram [2782, 2783] and similarly for tidal deformability [2784]. Also in the case of the two-families scenario, in which strange quark stars co-exist with neutron stars [2325], the existence of stellar objects having the same mass but different radii and tidal deformabilities is predicted [2785]. Sharp phase transitions thereby lead to very small values of tidal deformabilities and induce discontinuities in the tidal deformability-mass relation [294, 2481, 2482, 2786]. Current data are compatible with a phase transition in compact stars [2787–2791] and several indications could be found on its properties, e.g. it was concluded that a sizable quark core can exist inside a heavy NS ($\sim 2M_\odot$) [2789] or that strong phase transitions with a visible jump in the mass-radius relation are ruled out at 1σ at densities below 1.7 times saturation density [2792]. Agnostic studies also found a weak statistical evidence in favor of two stable branches with current data, that is, the existence of hybrid stars with a strong phase transition [2608, 2745];

JCAP03(2026)081

(iv) Concerning the constraints on empirical nuclear matter parameters, the results from NS observables have almost no effect on low-order parameters, the latter being mainly constrained (in the isoscalar sector) by nuclear physics information. A slight trend to favor "soft" EOS with relatively low values for $L_{\rm sym}$, $Q_{\rm sat}$ and $K_{\rm sym}$ has been observed without being conclusive [2662, 2746, 2793–2795].

In brief, current constraints remain inconclusive and a larger sample and higher precision measurements of NS properties together with inputs from subatomic physics are needed to advance our understanding of dense matter.

7.2.3 Reaction rates

Isolated mature NSs and NSs in the inspiral phase of BNS mergers are typically in near thermal and chemical equilibrium. As a result, knowing the EOS of dense matter is sufficient to relate its microphysical properties to the macroscopic parameters of NSs, such as mass, radius, tidal deformability. However, during the postmerger phase of BNS mergers and in core-collapse supernovae, including also the physics of ejecta and nucleosynthesis, matter is out of chemical (and thermal) equilibrium. In these scenarios, additionally reaction rates governing the various out-of-equilibrium processes are required to model the dynamics of these events and, ultimately, to extract information about subatomic physics from observations. This subsection provides a brief overview of the current state of the key ingredients needed to describe out-of-equilibrium processes. We will omit details about the precise implementation of these effects since there are many different ways to treat them, ranging from a simple source of dissipation within a hydrodynamics description to a full transport coupled to hydrodynamics via conservation equations (particle numbers, energy and momentum). The current incomplete understanding of these processes within dense matter and degeneracies with the EOS and other microphysical parameters limits our ability to draw definitive conclusions from future observations and will need to be improved to optimize the science returns with ET and multimessenger observations.

7.2.3.1 Neutrino rates. Neutrinos interact with matter through weak interactions. They reduce the lepton number of the system and affect the local cooling and heating via energy- and momentum transfer. Neutrinos play a central role in the dynamics of CCSN and largely determine the neutron-to-proton ratio in the ejecta of CCSN and BNS mergers, and thus the conditions for (heavy element) nucleosynthesis. Current and future neutrino observatories such as Super/Hyper-Kamiokande are capable of detecting neutrinos from an event in the Galaxy and its close environment. Understanding neutrinos in CCSN and BNS mergers is thus important for a better understanding of the multi-messenger emission by these transient events. Neutrino interactions are most important in the vicinity of the neutrinosphere, i.e., in the transition region from trapped neutrinos close to equilibrium to free streaming neutrinos which only feebly interact with matter. Although the exact location of the neutrinosphere depends on (anti-)neutrino energies and precise thermodynamic conditions, due to the strong variation of the reaction rates with temperature, the latter is often taken as indicator for the neutrinosphere with values in the range of a few MeV relevant for CCSN and BNS mergers.

JCAP03(2026)081

As a first approximation, the effect of neutrino absorption and creation processes can be included via its contribution to bulk viscous dissipation. Bulk viscosity from weak interactions is expected to be effective in damping post-merger density oscillations. The treatment of neutrino dynamics via a kinetic equation allows to include their reactions with the environment via opacities [2796]. These opacities can be utilized in various numerical schemes without assuming specific properties of the (anti-)neutrino distribution function, as is self-consistently determined from the transport equation. A full transport approach also enables the inclusion of other neutrino reactions such as scattering and pair creation via neutral current interactions. In addition, neutrino scattering processes could in principle provide viscosity to influence turbulent flow. Due to the large neutrino mean free paths, however, it is generally assumed that the magnetic field is much more efficient in this respect, see e.g. the discussion in [2797]. It should be noted that neutrinos influence matter properties locally, e.g. the temperature and composition, and its detailed impact on turbulence is not yet fully understood.

Bulk viscosities. The main weak reaction for bulk viscosity, first suggested in the study of cold matter [2798], arises from direct Urca processes describing neutron decay $n \to p + e + \bar{\nu}_e$, where $\bar{\nu}_e$ is the electron antineutrino, and the corresponding electron/positron capture or proton decay reactions. Recent research has extensively explored its contribution to bulk viscosity in both neutrino-trapped and transparent regimes in a hot and dense environment [2799–2803]. In addition, muonic Urca [2803] and modified Urca [2804], which involves bystander particles that contribute to energy-momentum balance, may contribute. Results for the bulk viscosity and damping timescales that cover the entire range of temperatures and densities are available in [2802, 2805] showing that bulk viscosity is most relevant at $T \sim 5\,\mathrm{MeV}$ where the transition between the trapped to untrapped neutrino regimes occurs. Bulk viscosities can be significantly enhanced due to resonant behavior [2806] and can arise due to phase conversion dissipation [2807] in NSs that also contain non-nucleonic matter.

Neutrino opacities within a transport approach. Approximating the effect of neutrino interactions via their contribution to (bulk) viscous dissipation implies averaging over neutrino phase space assuming free streaming. By contrast, neutrino transport allows to follow the dynamics throughout the system and thus requires information on the energy and angular dependence of the reaction rates. The importance of accurate neutrino transport in supernova simulations has spurred numerous studies of the relevant reactions. Nevertheless, it remains challenging to obtain reliable predictions. On the one hand this is due to the difficulties in determining the nuclear (strongly interacting) matrix element and on the other hand due to the computational cost of the high-dimensional phase space integration. The former clearly needs information beyond the EoS, starting with detailed information about the composition.

Concerning the different reactions, the direct Urca type reactions on nucleons contributing to bulk viscosity are in most cases the dominant ones for (anti-)neutrino absorption and creation and thus to determine the neutron to proton ratio, information lost within a viscous description. Opacities for these processes have been extensively studied in the literature, applying different levels of approximation for both matrix element and phase space integration, see e.g. [2808–2812]. At high densities, the predictions can vary by more than one order of magnitude, and depend strongly on the treatment of nuclear excitations.

JCAP03(2026)081

Under certain conditions, reactions on other particles such as hyperons or pions [2813] or in quark matter [2814, 2815], or involving muons as charged leptons [2816] can contribute as well. In the low-temperature limit, the direct Urca reactions are kinematically suppressed and the modified Urca processes which involve an additional particle for energy-momentum conservation must be considered, see e.g. [2804, 2817, 2818].

For neutrino-nucleon scattering kernels, different approximations for treating the nuclear interactions in dense matter have been considered, see e.g. [2808, 2809, 2819–2821]. In this case the level of approximation not only affects the opacity, but also influences the scattering angle distribution [2625]. In contrast to the modified Urca processes, the corresponding neutral current process, the Bremsstrahlung reaction, has received some attention in dense and hot matter [2822–2827] since it is known to influence neutrino spectra in CCSN. Electron capture (EC) on nuclei plays an important role during the late stages of stellar evolution and the pre-bounce phase of CCSN, see e.g. [2828]. Total EC rates are influenced both by the nuclear distribution and by the rates on individual nuclei, both of which suffer from uncertainties. The former is very sensitive to nuclear masses and for the latter, although microscopic calculations are available for a large number of different nuclei, see [2829] and references therein, the nuclei identified in several studies [2830–2832] as having the highest impact lie outside the region where microscopic calculations exist and parameterizations [2833, 2834] are often used. Theoretical and experimental efforts are underway to improve the situation and obtain reliable rates for all relevant nuclei [2835–2838]. Nuclear abundances also influence the neutrino opacity via neutrino-nucleus scattering [2839]. Standard rates for these reactions including in addition purely leptonic processes and plasmon decay are available in publicly accessible libraries like NuLib [2840] and Weakhub [2841].

7.2.3.2 Nucleosynthesis and reaction rates. As detailed in section 7.3.3, compact binary mergers involving at least one NS have been shown, both observationally and theoretically, to be a key astrophysical site for the production of neutron-rich nuclei by the rapid neutron-capture process (or r-process). Despite the recent success of nucleosynthesis studies for NS mergers, the estimated abundances and decay heat in the ejecta are still affected by a variety of uncertainties, including those associated with the complex nuclear physics description of exotic neutron-rich nuclei. R-process nucleosynthesis calculations require a reaction network consisting of about 5000 species from protons up to $Z \simeq 110$ lying between the valley of β-stability and the neutron drip line [2842, 2843]. All charged-particle fusion reactions on light and medium-mass elements that play a role when the nuclear statistical equilibrium freezes out need to be considered, in addition to radiative neutron captures and photodisintegrations. On top of these reactions, β-decays as well as β-delayed neutron emission probabilities and α-decay rates need to be taken into account, but also fission processes, such as neutron-induced, spontaneous, β-delayed and photofission, together with the corresponding fission fragment distribution for all fissioning nuclei. All rates should ideally be based on experimental information whenever available, but since only an extremely tiny amount of data concerning the neutron-rich nuclei produced during the r-process are known experimentally, theoretical models are fundamental.

For the estimate of reaction and decay rates of relevance in r-process simulations, the necessary nuclear ingredients (properties of cold and hot nuclei, nuclear level densities, optical

JCAP03(2026)081

potentials, γ-ray strength functions, fission properties, β-strength functions) should ideally be derived from *global*, *universal* and *microscopic* models [2844]. Nowadays, microscopic or semi-microscopic mean-field-type models can be tuned to the same level of accuracy as the phenomenological models, and therefore could replace the phenomenological inputs in astrophysical simulations [2845]. Some details about existing models to estimate the key ingredients to nucleosynthesis reaction network calculations are given below. They concern nuclear masses, β-decay and reaction rates.

Nuclear masses. Among the properties of ground state matter, the atomic mass is the most fundamental quantity (for a review, see e.g. [2846]) and governs the r-process path through the competition between inverse channels like the dominant (n,γ) and (γ,n) reactions. Uncertainties in the mass predictions may significantly affect the r-process predictions and consequently the ejecta composition and decay heat resulting from NS merger [2847]. When not available experimentally [2848], these quantities need to be extracted from a mass model which aims at reproducing measured masses as accurately as possible, i.e typically with a root-mean-square (rms) deviation smaller than 800 keV. Modern mass models not only try to reproduce experimental masses and mass differences, but also charge radii, quadrupole moments, giant resonances, fission barriers, shape isomers, infinite nuclear matter properties, and more [2846, 2849].

Nowadays, nuclear structure properties can be accurately determined within the (relativistic or non-relativistic) mean-field model [2850]. This is a variational approach in which the trial wavefunction of the nucleus has the form of a Slater determinant of single-particle wavefunctions. The energy is then calculated by minimizing the expected value of the Hamiltonian with respect to arbitrary variations in the single-particle wavefunctions. Since the mean field itself depends on these wavefunctions, the process has to be reiterated until an acceptable level of self-consistency is reached. Such non-relativistic Hartree-Fock-Bogolyubov calculations based on the Skyrme zero-range [2851, 2852] or Gogny finite-range [2853] effective interactions have proven their capacity to describe experimental data, provided the interaction parameters are directly fitted to the complete set of known masses. The accuracy achieved by relativistic mean field models also still needs to be improved, as the most successful interaction still leads to rms deviations larger than about 1.2 MeV. Other global mass models have been developed, essentially within the so-called liquid drop or droplet approach, where the binding energy is macroscopically described by the leading volume and surface terms as well as a symmetry energy (also with a volume and surface contribution) and a Coulomb energy. Microscopic corrections to account for quantum shell and pairing correlation effects need to be added to the liquid drop part [2846]. Despite its success, this macroscopic-microscopic approach remains unstable with respect to parameter variations, especially when approaching the neutron drip line, and suffers from major shortcomings, such as the incoherent link between the macroscopic part and the microscopic correction or the instability of the shell correction [2846, 2849].

β-decay rates. β-decay rates are fundamental in much of nuclear astrophysics [2854, 2855], particularly so in r-process nucleosynthesis [2842, 2843] for which they set the timescale of the nuclear flow and consequently of the production of the heavy elements [2847]. Most

JCAP03(2026)081

of the nuclei involved during the r-process neutron irradiation have yet to be discovered, with β^--decay half-lives known only for about 1200 nuclei [2856]. A proper prediction of r-abundances in any r-process site calls for β-decay rates to be estimated within a factor smaller than typically 1.5. However, only a restricted number of global models of β-decay rates are available for nucleosynthesis applications [2857–2861] and deviations between their predictions can reach factors of 100 for many neutron-rich regions. In particular, for very heavy $Z \gtrsim 82$ nuclei, as well as along the isotonic chains corresponding to closed neutron shells ($N = 50, 82, 126, 184$), responsible for the formation of the r-process peaks observed in the solar system, non-negligible differences can be observed, leading to different estimated r-process peak structures [2862].

More effort is needed in the future to include not only the contribution of the forbidden transitions [2859, 2860] but also deformation effects, as the majority of nuclei is expected to be deformed [2863]. Recent studies within the fully self-consistent proton-neutron Quasi-particle random phase approximation (QRPA) model using the finite-range Gogny interaction have now also consistently taken axially symmetric deformations into account [2863], but forbidden transitions remain to be included. The inclusion of finite-temperature effects as well as the phonon coupling has also been shown to give rise to a redistribution of the QRPA strength and significantly impact the β-decay half-lives of neutron-rich nuclei [2864]. Inclusion of particle-vibration coupling effects has also been shown to redistribute the Gamow-Teller strength and impact the β-decay half-lives of neutron-rich nuclei significantly [2865]. Finally, note that on the basis of the β-decay strength, the β-delayed processes, including neutron emission and fission for the heaviest species, need to be derived. Detailed calculations on the basis of statistical reaction codes, like TALYS [2866], can account for the competition of the various open channels (neutron, photon, fission) in the daughter nucleus. Reaction models still need to be better exploited to estimate the probability for such β-delayed processes.

Neutron capture rates. If an $(n, \gamma) \rightleftarrows (\gamma, n)$ equilibrium is established during the r-process, the abundances and decay heat in the ejecta of NS mergers remain rather insensitive to the adopted reaction rates. However, even in this case, i.e. to prove that an $(n, \gamma) \rightleftarrows (\gamma, n)$ equilibrium is achieved, it is necessary to estimate the rates and perform network simulations to show that neutron captures and photoneutron emissions are faster than β-decays in the conditions prevailing during NS mergers. If an $(n, \gamma) \rightleftarrows (\gamma, n)$ equilibrium is not established, as expected in particular at late times when reactions freeze out, the abundances become directly sensitive to the estimated rates.

Most of the low-energy cross section calculations for nucleosynthesis applications are based on the statistical model of Hauser-Feshbach. The statistical model has proven its ability to predict cross sections accurately for medium- and heavy-mass nuclei. However, this model suffers from uncertainties that essentially stem from the predicted nuclear ingredients describing the properties of the nuclear ground and excited states, the γ-ray strength function and the optical potential. Nuclear level densities typically affect rates by a factor of 10 with a strong odd-even effect (i.e. between systems with an even or odd number of nucleons) according to the way the pairing interaction is treated. The γ-ray strength function may impact the prediction of the rate up to a factor of 100, in particular depending on the description of the low-energy tail of the giant $E1$ resonance, or if the low-energy $M1$ component is included,

JCAP03(2026)081

both for the scissors mode and its low-energy enhancement related to the de-excitation mode (also referred to as the $M1$ upbend) [2867, 2868]. Finally, the optical potential is known to have a negligible impact in the standard case of radiative neutron captures. However, a reduction of the imaginary component of the neutron-nucleus potential (that takes into account the absorption of the reaction flux from the elastic channel) may have a drastic impact in reducing the capture cross section by neutron-rich nuclei. More details on our capacity to reliably predict all these ingredients can be found in [2844, 2854, 2867, 2869–2872].

In addition, at the very low energies of astrophysical interest for light or exotic neutron-rich nuclei for which few, or even no resonant states are available, the capture reaction is known to be possibly dominated by direct electromagnetic transitions to a bound final state rather than through a compound nucleus intermediary. This direct contribution to the neutron capture rate can be 2–3 orders of magnitude larger than the one obtained within the statistical approach traditionally used in nucleosynthesis applications [2844, 2873–2875]. Significant uncertainties still affect the predictions of the direct contribution. These are related to the determination of the nuclear structure ingredients of relevance, i.e., the nuclear mass, spectroscopic factor, neutron-nucleus interaction potential and excited level scheme. A special emphasis needs to be put on determining the low-energy excitation spectrum with all details of the spin and parity characteristics. This can be deduced from a nuclear level density model, but not a statistical approach. Further efforts are needed to improve the prediction of such nuclear inputs within reliable microscopic models. The transition from the compound to the direct nucleus mechanism when only a few resonant states are available also needs to be tackled in a more detailed way, for example within the Breit-Wigner approach [2876].

In view of all the above-mentioned difficulties and complexities of the relevant nuclear physics, the estimate of nuclear masses, β-decay and neutron capture rates of exotic neutron-rich nuclei need to be further improved, both experimentally and theoretically, in order to be able to accurately estimate the ejecta composition and decay heat released by compact binary objects after merger. Future kilonova light curve and spectra observations, triggered by ET detection of NS-NS and NS-BH systems, will provide constraints on the r-process nucleosynthesis provided nuclear physics uncertainties are significantly reduced.

7.3 Prospects for constraints on microphysics with ET data

We expect that in the near future our current understanding of the various fundamental phenomena related to the astrophysics of NSs will be improved thanks to a new generation of telescopes and advanced GW detectors. New observational data both in pre- and post-merger phases will be of great help for understanding their internal composition, thermal effects, and nucleosynthesis. This will significantly contribute to insights in the internal structure of compact objects, dynamics of their mergers, and explosion mechanisms of CCSNe. In this context, an important line of work for ET will be to assess the possibility of finding a phase transition to "exotic", i.e., non-nucleonic, matter inside NSs. In this section wediscuss the capabilities of ET. In section 7.3.1 we review the possibilities to obtain constraints on low temperature matter, in section 7.3.2 on the postmerger phase of a BNS or on hot matter from CCSN, respectively, and in section 7.3.3 on multi-messenger aspects. For the following

JCAP03(2026)081

discussion we assume general relativity as theory of gravity; see section 7.4 for a discussion of the impact of alternative theories on the subatomic physics outcome.

7.3.1 Constraints on low-temperature microphysics

7.3.1.1 Compact Binary Mergers (NS-NS and NS-BH). As discussed in section 7.2.2, current measurements are insufficient to answer fundamental open questions on the properties of dense baryonic matter and the occurrence of phase transitions, possibly to deconfined quark matter in the core of NSs. With current detectors, we expect at most ten to hundred NS-NS or NS-BH mergers per year [392, 2187], whereas ET will enable the detection of up to 10^5 BNS mergers per year [15]. The enhanced sensitivity will also lead to higher precision measurements of tidal deformability and sub-dominant matter effects during inspiral. In addition, in mixed (NS-BH) binaries, tidal forces on the NS can become so strong that it gets tidally disrupted, which leads to a distinctive sudden shutoff of the GW signal. The disruption occurs at a characteristic frequency in the O(kHz) range that depends primarily on the NS compactness, BH mass and spin [1471, 2877, 2878] and thus yields additional, clean information on the cold EOS, though spin precession may complicate the identification of the shut-off [2879]. ET will be able to detect NS-BH binaries out to redshifts of ~ 20 [15, 1167], which leads to a noticeable shift in the detected GW frequencies. For a fraction of these observable events, the NS will be tidally disrupted, which would only be detectable for events with a sufficiently high signal-to-noise ratio (SNR).

In addition, information on microphysics in and beyond the EOS could come from the characteristic oscillation modes excited by the tidal field of the companion in a binary system, or by other mechanisms in isolated NSs (see e.g. ref. [2773]). The most relevant modes from the observational point of view and to obtain spectroscopic information about the NS interior are the fundamental (f), the gravity (g), and r modes that lead to imprints in the GW signal. The f-modes have the strongest tidal couplings and their behavior below resonance is the primary contributor to the tidal deformability discussed above. For slowly rotating NSs, these modes have frequencies in the kilo-Hertz range, making their effects most significant near the end of the inspiral in circular orbits. However, high spin can lower the mode frequency, allowing these excitations to occur earlier in the inspiral, potentially even reaching resonance before the plunge or merger phase (see, e.g., [2880, 2881]). Gravity g-modes and related classes of interfacial modes are directly associated with steep composition gradients in the NS, and arise, for instance, from a strong phase transition, with their frequencies and amplitudes containing direct information about the properties of the transition. The r-modes have frequencies proportional to the spin of the NS and may thus become excited during the early inspiral. Although their effects could be relevant for ET, their influence will likely be subdominant to f-mode effects due to the significantly weaker tidal coupling [2882, 2883]. The low-frequency sensitivity of next-generation detectors will be key to capture this information in loud events. It is also important to note that f- and r-mode excitations have opposite effects on the merger timing, with f-modes advancing and r-modes delaying the merger [2882, 2884]. In addition, various kinds of spin-tidal couplings [2885] will enrich the subdominant GW signatures during binary inspirals. Moreover, effects of viscosity may also play a role, in particular in conjunction with tidal heating due to mode

JCAP03(2026)081

excitation [2886–2889]. Together, these effects can influence the oscillation spectra [2890–2893] and the tidal response function [2894–2896]. Modes can also play an important role in single NSs for continuous gravitational wave (CGW) signals and in the proto-NSs formed in SNe, as will be discussed in sections 7.3.1.2 and 7.3.2.2, respectively.

As discussed above, the connection between astrophysical observations and microphysical properties of NSs requires both microscopic and macroscopic (global simulation) modeling, where the specific microphysics inputs depend on the astrophysical scenario explored. If one restricts the study to cold, non-rotating, and unmagnetized NSs, which are the subject of this section, this connection mainly relies on the knowledge of the EOS [pressure versus energy density relation $P(\varepsilon)$] of cold (baryonic) matter in β-equilibrium (see section 7.2). For static properties of NSs, the hypothesis of validity of general relativity (see section 7.4.3 for a discussion about possible consequences when relaxing this assumption) suffices to guarantee a direct correspondence between global properties and the corresponding EOS. Therefore, it is, in principle, possible to reverse the problem and associate to simultaneous observations of the M-Λ relation of several NSs the underlying EOS. The measurement of mass and radius of several NSs with high precision as projected by X-ray telescopes, successors of NICER, are very promising in this respect, too (see e.g. [2897] for a review), but suffer from larger modeling uncertainties. However, intriguing degeneracies should be noted in this context. Very similar M-R relations can be obtained under different hypotheses on the underlying microphysics, giving rise to the so-called "masquerade" effect [2898], where hybrid stars involving a quark matter core can be difficult to distinguish from those comprising only hadronic matter. Another potential degeneracy are so-called tidal deformability doppelgängers [2899], which have been found in sets of parameterized EOS models when allowing for a strong first-order phase transition at low density of $1 - 2n_{\rm sat}$. Such doppelgängers can have similar tidal deformabilities (as well as main postmerger frequencies) that are indistinguishable within the statistical uncertainties achievable by current GW detectors but different radii. The use of more restrictive prior information from nuclear physics and joint EOS interpretations with astrophysical measurements of NS radii could reduce these degeneracies.

More and higher-precision measurements such as those expected from ET will contribute to reduce the error bars, thus tightening the constraints on the EOS [16]. In this section, we discuss constraints on the low-temperature microphysics that can be obtained from (future) binary-merger GW data. They concern information inferred from the pre-merger phase, when matter can still be assumed as 'cold', while constraints on the finite-temperature EOS, which is relevant for the post-merger phase or CCSN, will be discussed in sections 7.3.2.1 and 7.3.2.2, respectively.

Constraints on hadronic EOS parameters and composition. Several studies have been performed highlighting the potential of next-generation GW observatories, such as ET, for constraining the NS EOS. First of all, those observatories will not only detect many events but, due to higher sensitivity, also more precisely determine the component masses and the mass-weighted tidal deformability $\tilde{\Lambda}$; see, e.g., for recent works refs. [16, 1231, 2467, 2900, 2901].[62]

[62]The mass-weighted tidal deformability is defined as [1225]

$$\tilde{\Lambda} = \frac{8}{13}\left[(1+7\eta-31\eta^2)(\Lambda_1+\Lambda_2) + \sqrt{1-4\eta}(1+9\eta-11\eta^2)(\Lambda_1-\Lambda_2)\right] , \tag{7.5}$$

JCAP03(2026)081

N_{ET}	$\Lambda_{1.4M_\odot}$		$\Lambda_{2.0M_\odot}$	
	BSk24	Nl3$\omega\rho$	BSk24	Nl3$\omega\rho$
10	$550.590^{+39.262}_{-36.078}$	$914.771^{+26.206}_{-33.372}$	$61.438^{+11.460}_{-11.137}$	$108.683^{+12.474}_{-10.709}$
50	$526.677^{+19.882}_{-19.022}$	$935.696^{+1.357}_{-4.151}$	$51.473^{+7.854}_{-6.402}$	$114.872^{+0.084}_{-0.084}$
100	$518.230^{+22.086}_{-23.094}$	$934.407^{+0.069}_{-2.862}$	$45.306^{+6.521}_{-8.030}$	$114.287^{+0.670}_{-1.116}$
500	$513.879^{+1.405}_{-2.147}$	$931.547^{+0.002}_{-0.002}$	$37.722^{+0.445}_{-0.780}$	$114.957^{+0.0003}_{-0.0003}$
1000	$505.346^{+9.939}_{-4.168}$	931.545^{+5e-6}_{-5e-6}	$38.893^{+0.733}_{-1.616}$	114.957^{+5e-7}_{-5e-7}
2000	$511.192^{+0.540}_{-0.540}$	931.545^{+4e-8}_{-4e-8}	$37.170^{+0.228}_{-0.228}$	114.957^{+3e-9}_{-3e-9}
5000	$512.294^{+0.528}_{-0.528}$	$931.545^{+1e-13}_{-1e-13}$	$37.293^{+0.349}_{-0.349}$	114.957^{+0}_{-0}

Table 12. Mean and 1σ statistical uncertainties on tidal deformability for $1.4M_\odot$ and $2.0M_\odot$ NSs with varying number of simulated detections using BSk24 and Nl3$\omega\rho$ EOS models for injection, as depicted in left panel of figure 124.

Assuming a relatively broad mass distribution in NS binaries, this leads to a determination of $\tilde{\Lambda}$ as function of the two masses, which in turn allows obtaining the mass-tidal deformability relation. This can be translated into constraints on the NS EOS and hence NS radii. The capability of ET to access lower frequencies can also contribute to increasing the precision of the parameter estimation, although this effect is more important for determining the chirp mass and the mass ratio than on the measurement of the tidal deformability [16].

The added value of multiple detections with ET is shown in the left panel of figure 124 (adapted from ref. [1231]), where the extracted value of the tidal deformability for a $1.4M_\odot$ and a $2M_\odot$ NS is shown for an increasing number $N_{\rm ET}$ of detections with ET, see table 12 for the corresponding mean values and 1σ uncertainties. A uniform distribution for NS masses between $1.1M_\odot$ and the maximum mass for each EOS has been assumed and the events are chosen randomly among the events leading to a $\tilde{\Lambda}$ measurement from the simulation of detected BNS merger events with ET over one year from ref. [1231]. Compared to the total number of $\sim 10^5$ BNS merger detections expected par year with ET, those with $\tilde{\Lambda}$ measurement correspond — depending on the injected EOS and the waveform model used — to roughly 60–70% of the total number. For a discussion of the influence of different detector configurations on these expected detections, see section 10.3.4.

Note that the capability to determine the tidal deformability of a star with a given mass, and thus to infer the NS EOS and radius, will depend on the mass distribution of the measured events — detections of events across a wide range of masses will better constrain the EOS for a large range of densities. For EOS inference, a nucleonic meta-modeling approach has been employed within a Bayesian framework [2746, 2902]. With $\gtrsim 500$ detections, the underlying NS EOS can be narrowed down quite accurately irrespective of the different proposed designs (2L shape or triangle) of ET. Without doppelgängers, NS radii for the fiducial masses can also be determined from this analysis [1231]. To be precise, in this case the uncertainty on radius and tidal deformability is reduced from (1–2)% for $N_{ET} = 10$ to less

where Λ_1 and Λ_2 are the tidal deformabilities of the two component stars, and $\eta = m_1 m_2/(m_1+m_2)^2$ is the symmetric mass ratio. The usefulness of $\tilde{\Lambda}$ is that it is the combination that enters the inspiral waveform at 5 PN order, where tidal effects first appear.

JCAP03(2026)081

than $10^{-3}\%$ for $N_{ET} = 5000$. This is in agreement with other studies, e.g., that in ref. [2903], where it was shown that a few loud events within a network of next-generation observatories are sufficient to determine radii with a precision of < 100 m. It should be noted that the difference of applying a unified crust model or a fixed reasonable unique crust does not induce any noticeable difference in the above analysis if the latter is matched consistently at the corresponding crust-core transition and reasonably well describes the crust [2723] even for ET. This result might seem astonishing on a first sight in view of the large differences obtained for the predicted radii for some EOS models between unified and unique crust [2628, 2804]. The reason is probably that recent constraints from nuclear theory, in particular from χEFT, very strongly constrain the EOS in the crust region [2723].

Most of these constraints can be derived from the measurement of BNS systems; however, NS-BH systems can also provide valuable information about the EOS. Those constraints would mainly arise from observations of NS-BH systems in which the objects have comparable masses and/or the BH is highly spinning, see e.g. [2904, 2905].

Concerning the underlying nuclear matter parameters, it should be noted that there is some degeneracy and that different combinations of parameters lead to the same EOS for β-equilibrated NS matter, and thus, measuring the tidal deformability alone does not determine all nuclear matter properties [1231, 2771, 2906]. Similar conclusions have been drawn for precise NS radius measurements [2907]. However, with some complementary information either from independent observations or from nuclear physics experiments or theory, ideally on symmetric (i.e., same number of neutrons and protons) matter, nuclear matter properties can be determined very precisely. To cite some examples, within a given framework for the nuclear Hamiltonian, refs. [2908, 2909] found that next-generation observatories have the potential to constrain the strength of the three-nucleon interaction. Complementary information on the low-temperature EOS from the inspiral phase could also come from combined measurements of the tidal deformability and quadrupolar crust-core interface i-modes through multi-messenger astronomy (specifically, through resonant shattering flares). Indeed, even if i modes are expected to be weak, their detection might be within reach for ET, and ref. [2910] suggest them as a possible way to constrain the empirical nuclear matter parameters with a single loud event being sufficient. As discussed above, exotic hadrons may also be present. The GW signatures of a strong phase transition that could reveal their presence is discussed below; in addition they would likely also impact viscosities, which may be constrained from signatures in GWs from binary inspirals, e.g. [2895, 2896].

Altogether, these studies demonstrate the unprecedented potential of detectors such as ET to determine from the inspiral of BNS mergers the underlying NS EOS, and help to constrain NS structure and properties of dense matter.

Comparison between triangular and 2L-configurations. Given the current situation in which the final choice for ET geometry has not yet been made, it is important to also consider the impact of different designs and configurations on the science return regarding the EOS inference; since the parameters encoding most information about the EOS are the masses and tidal deformabilities, in the following we will focus on these when discussing the difference between a triangular ET with 10km arms vs. 2 L-shaped detectors with 15km arms; a

JCAP03(2026)081

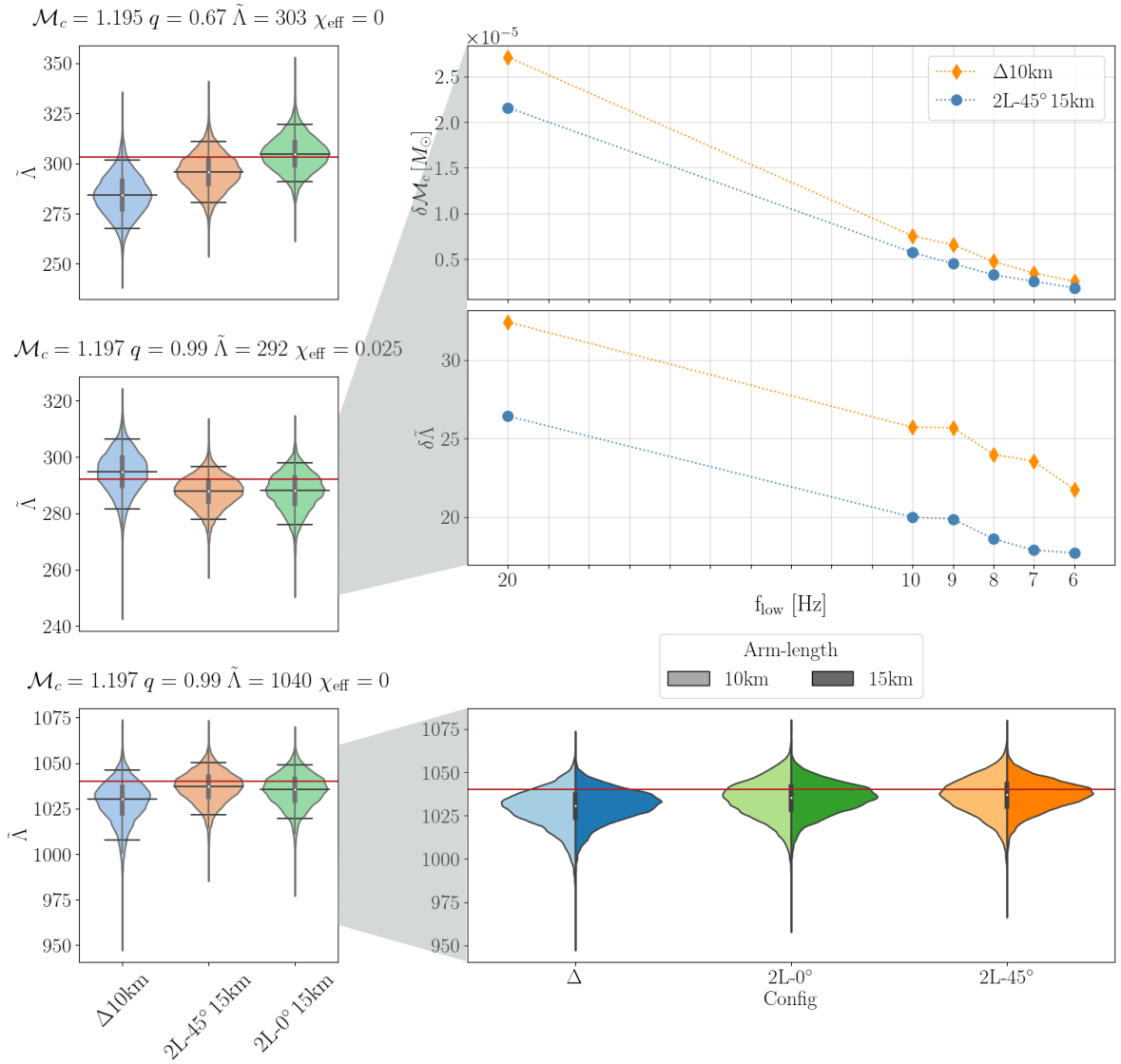

Figure 122. *Left:* $\tilde{\Lambda}$ posteriors recovered from the simulated signals for three different sources, whose parameters are reported on top of each panel, for three ET configurations; the horizontal red line indicates the injected value. Right-top panel: width of the 90% confidence interval of the $\mathcal{M}_c$ and $\tilde{\Lambda}$ posteriors obtained for the source in the middle on the left-hand side panels, when performing the analysis with different starting frequencies $f_{\rm low}$; the different markers and colors correspond to two different detector configurations. Right-bottom panel: $\tilde{\Lambda}$ posteriors recovered for the source on the bottom panel on the left-hand side, with the red line showing the injected value; th different colors correspond to the different ET geometries, with the lighter shade representing a 10 km arm-length configuration, and the darker ones a 15 km arm-length one. See ref. [2901]. Reprinted figure with permission from [2901], Copyright (2023) by the American Physical Society.

detailed comparison can be found in [16]. We also refer to chapter 10 for similar studies employing a Fisher matrix approach.

Figures 122 and 123 show an example of how accurately we expect to infer these quantities from complete PE runs with ET. Figure 122 shows a summary of the results presented in

JCAP03(2026)081

refs. [16, 2901], to which we refer for more details. The panels on the left-hand side show the posteriors obtained for $\tilde{\Lambda}$ from mock signals created for three different sources, all placed at a distance of 100 Mpc, with three possible ET configurations: a triangle with 10 km arm-length (Δ), placed in Sardinia, or two L-shaped interferometers with 15 km arm-length, one in Sardinia and one in Limburg, with either aligned ($2L - 0°$) or misaligned ($2L - 45°$) arms; in all cases the sensitivity for the xylophone configuration in cryogenic mode was considered. For all sources, all configurations recover $\tilde{\Lambda}$ very well. The posteriors for Δ seem slightly wider than the 2L ones. In order to check whether this is due to the geometry or the arm-length, for one of the sources we repeated the analysis for all the configurations with 10 km and 15 km arm-length. As shown in the bottom panel on the right-hand side of figure 122, if we compare detectors with the same arm-length, the obtained precision on $\tilde{\Lambda}$ is the same. Finally, the top panels on the right-hand side show the width of the 90% confidence interval of the chirp mass $\mathcal{M}_c$ and mass-weighted tidal deformability $\tilde{\Lambda}$ posteriors for the analysis performed at different starting frequencies $f_{\rm low}$, highlighting how, irrespective of the configuration, the increased sensitivity of ET at lower frequencies will help in obtaining more and more accurate measurements of these parameters. Figure 123, instead, compares how accurately we measure $\tilde{\Lambda}$ for high-SNR simulated signals from a catalog of 100 sources with a triangular or two L-shaped detectors, showing the difference between the 90% confidence interval obtained from the analysis considering one triangular detector with 10 km arm-length (placed in Limburg) or two L-shaped, misaligned detectors, with 15 km arm-length (one placed in Sardinia and one in Saxony). As a caveat, these inference runs were not performed as a "standard" PE run, since the work for which they were produced included six additional free parameters to model the tidal phase in a model agnostic way in the Bayesian inference, which causes the posteriors to be wider than we would have with regular PE. However, figure 123 shows clearly how in most cases the 2L configuration recovers more accurate posteriors for both $\tilde{\Lambda}$ and $\mathcal{M}_c$.

Constraints on a potential phase transition. As discussed in section 7.2.2, there are clear features in the mass-tidal deformability relation which are a signature of a phase transition. To identify them, or to break possible degeneracies, the resolution and statistics achievable with next-generation observatories is required. We note that they only depend on the thermodynamic characteristics of the phase transition and not on the details of the two adjacent phases. Thus, although the most studied case is a transition from hadronic to deconfined quark matter within NS, a detection of a phase transition would not be a proof of a quark matter core. As discussed below, detecting signatures from g-modes directly associated to the transition could supplement additional information, however, more work is needed to fully explore the information contained in their GW signatures.

The detectability of a phase transition from the inspiral of a BNS merger with next-generation observatories has been the subject of numerous works recently. For instance, based on the breakdown of quasi-universal relations fitted to purely hadronic EOS in [2911] and a comparison of the inferred radius in [2912] together with a collection of simulated events for a few purely hadronic and hybrid EoS, the authors suggest that $\sim 50 - 100$ detections can be sufficient to distinguish different EoSs. Similar findings, showing that, under some conditions, a relatively small number of events — reachable with ET with a single week of operations — could be sufficient to infer on a first-order phase transition, have been obtained in others

JCAP03(2026)081

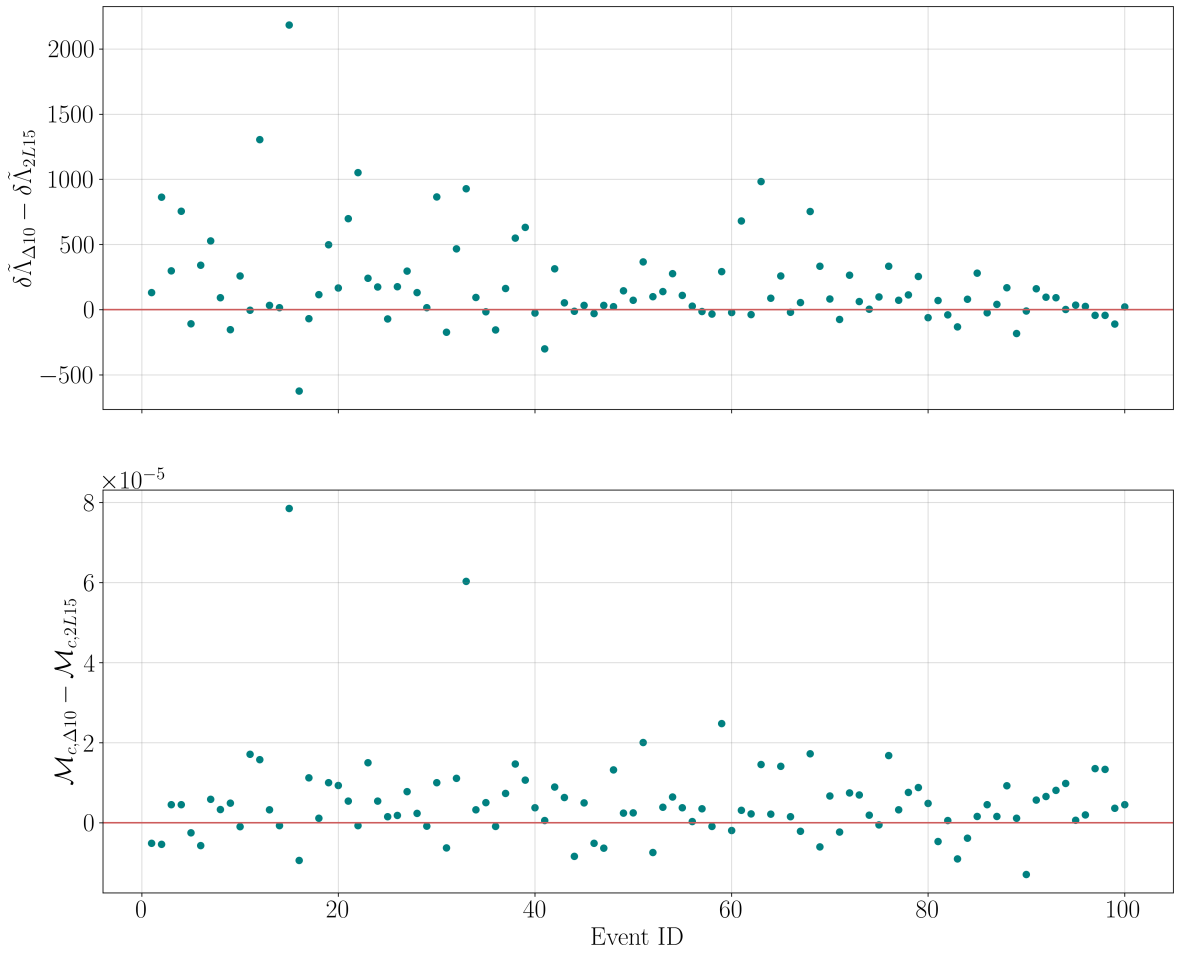

Figure 123. Difference between the width of the 90% confidence interval obtained with a triangular, 10 km arm-length detector and a configuration including two L-shaped interferometers with 15 km arm-length, for the posterior recovered for $\tilde{\Lambda}$ (top panel) and $\mathcal{M}_c$ (bottom panel), over a catalog of simulated signals for 100 different sources. The red line marks zero, meaning that points above (below) the line show a wider posterior for the Δ (2L) configuration.

studies using Bayesian non-parametric EOS inference [2913, 2914]. This conclusion relies on the fact that the uncertainty on the tidal deformability is significantly reduced if multiple BNS mergers are detected, as shown in the right panel of figure 124 (adapted from ref. [2914]).

The most complete investigation to date, which was based on representing the full variation of the nucleonic EOSs and phase transitions within a meta-modeling approach (see section 7.2.1), concluded that from a single loud event of BNS merger up to a luminosity distance $\lesssim 300$ Mpc, a phase transition at relatively low density (around twice saturation density), can be successfully identified [2485]. In this study, the phase-transition signal was quantitatively extracted through Bayes factors, assuming the simulated precision in the tidal deformability that would be achieved by ET.

Moreover, using a large sample of hybrid EOSs with a first-order phase transition to deconfined quark matter, ref. [2915] showed that the detection of a system with a total binary mass equal to the threshold mass for prompt black hole formation, together with the

JCAP03(2026)081

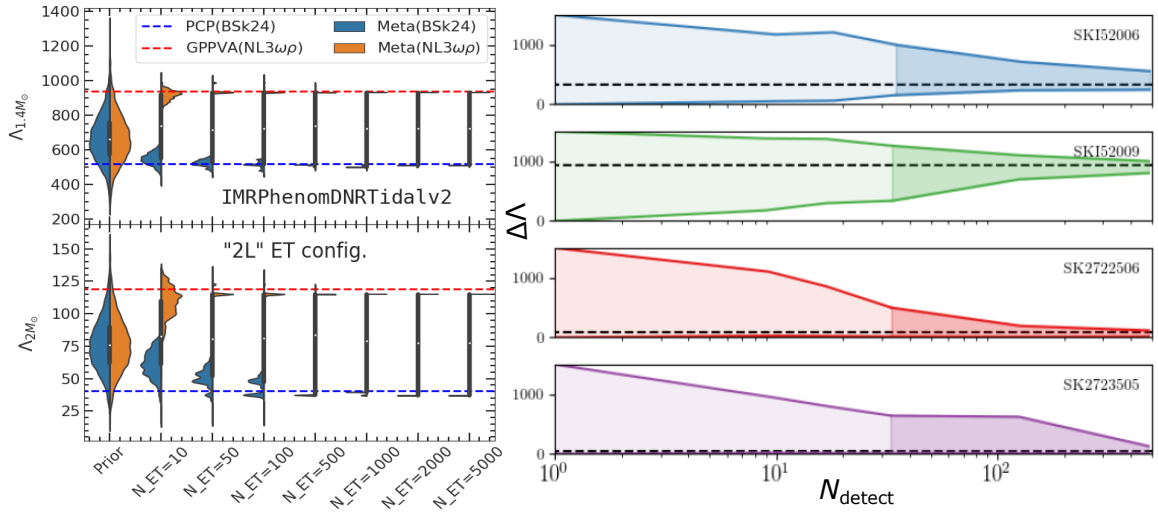

Figure 124. *Left panel:* increased precision obtained from multiple ET detections of the tidal deformability for a $1.4M_\odot$ and $2.0M_\odot$ NS using a nucleonic meta-modeling technique (violin shapes); for comparison the prediction of two selected EoSs is shown with horizontal lines. *Right panel:* reduction in the uncertainty on the tidal deformability with increasing number of detection. Figures reprinted figure with permission from [1231], Copyright (2023) by the American Physical Society (left) and reproduced from [2914]. CC BY 4.0 (right panel).

(combined) measurement of the dimensionless mass-weighted tidal deformability $\tilde{\Lambda}$ and the threshold mass, could reveal the possible appearance of a phase of deconfined quark matter in NSs. With the large number of events expected with ET, such a detection seems possible.

In addition, phase transitions modify the spectrum of oscillation modes of the NS. In particular, the principal core g-mode in hybrid stars containing quark matter has an unusually large frequency range compared to ordinary NSs of the same mass [2916]; as such, for binary mergers involving at least one hybrid star, the fraction of tidal energy pumped into resonant g-modes can exceed the corresponding energy of a normal NS by a factor of 2 to 3 [2916]. Likewise, the resonant tidal excitation of g-modes due to a transition from nucleonic to hyperonic matter can potentially be measurable with detectors such as ET [2917].

In conclusion, these studies highlight the enormous potential of ET to answer open questions such as the occurrence of phase transitions in NSs and the need to complement this information by other observables to fully understand not only the dense matter EOS in β-equilibrium, but its inner structure and behavior for other conditions.

7.3.1.2 Continuous GWs.

Neutron star mountains. Rotating NSs that support long-lived, non-axisymmetric deformations, colloquially known as *mountains*, have long been considered interesting sources of continuous GWs. Even though the amplitude from such a source is likely to be weak, one may hope to integrate over long-lasting continuous waves to gain in signal-to-noise ratio. Considerable effort has gone into modeling and searching for GWs from deformed rotating NSs. This effort has not yet been rewarded with success. Searches have only provided upper limits on the size of the involved deformations. However, we are beginning to probe the

JCAP03(2026)081

interesting parameter regime and with the improvements in detector sensitivity and analysis techniques anticipated in the era of next-generation instruments, there are good reasons to expect observations, see e.g. [16]. This motivates a closer discussion of the physics involved in the problem and the observational effort associated with it.

Why should we expect NSs to support mountains in the first place? The answer is quite simple, even though the precise details are not. The formation history of a NS starts from the remnant of a supernova. A newly born NS will be hot and rapidly rotating, as it retains some of the angular momentum of the progenitor star (or is given a "kick" during the collapse process [2918]). As the star cools, it becomes energetically favourable to form a crystal lattice at low densities and the crust forms. The NS may then, at some point in its lifetime, exhibit starquakes/glitches or accrete from a companion star. These processes are expected to build up (or release) strain in the crust and cause the star to change shape. Intuitively, it seems inevitable that a typical NS will be deformed in a non-axisymmetric fashion and therefore *should* emit GWs.

The general problem of deformed NSs has been reviewed in [2919–2922]. These discussions include mountains, but also long-lived oscillation modes, like the r-modes (discussed later) which may be excited and radiate GWs. The problem of detecting the continuous GW signals from NSs is reviewed in [2216, 2923–2929].

In general relativity (and if we ignore internal dynamics) an isolated body must spin and be deformed away from axisymmetry in order to radiate GWs — there must be a time-varying quadrupole moment [559]. The fact that NSs have solid crusts close to the surface enables them to support long-lived, non-axisymmetric deformations. These deformations can be quantified in terms of the principal moments of inertia, I_j. For a rigid uniformly rotating star with angular velocity Ω about the $z = x^3$-axis, an estimate of the strain amplitude is:

$$h_0 = \frac{4G}{c^4}\frac{\epsilon I_3 \Omega^2}{d} \approx 10^{-25}\left(\frac{10\text{kpc}}{d}\right)\left(\frac{\epsilon}{10^{-6}}\right)\left(\frac{I_3}{10^{45}\,\text{g}\,\text{cm}^2}\right)\left(\frac{\nu}{500\,\text{Hz}}\right)^2, \tag{7.6}$$

where $\nu = \Omega/2\pi$ is the star's spin frequency and we have defined the *ellipticity* of the star as

$$\epsilon \equiv \frac{I_2 - I_1}{I_3}. \tag{7.7}$$

The ellipticity is a dimensionless measure of the star's quadrupolar deviation from symmetry about the z-axis. From eq. (7.6) we see that, even for a reasonably nearby and rapidly rotating source, the GW strain is extremely weak. However, if the source can be observed for a sufficiently long period of time, the strain data measured at the detector can be folded over itself to improve the signal-to-noise ratio (roughly as the square root of the observing time for fully coherent searches or as the fourth root of the observing time for semi-coherent searches [2927]). We also see that the detection problem is degenerate. We need, for example, some insight into the moment of inertia, whose value is uncertain up to a factor of 3–5, depending on the NS mass and EOS [2930].

In an all-sky search for unknown GW sources, i.e., those sources for which no corresponding EM signal is observed, a signal with some given amplitude will not allow us to infer ϵ and constrain the relevant nuclear physics, e.g. the crustal strength, unless additional information, e.g., the distance, is available. Instead, focusing on known NSs for which an estimated

JCAP03(2026)081

distance and an observed spin-down rate is available, we can work out the required energy loss. Assuming that the energy is entirely radiated through GWs we have an upper limit on the NS mountain. This estimate — the so-called spin-down limit — allows us to quantify to what extent known pulsars could in principle be detectable GW sources. figure 125 provides an illustrative example, showing the minimum required ellipticity for known pulsars and two specific ET configurations. The estimates do not change much among the two possible instrument designs, see section 8 for a more detailed discussion. However, we know that some energy is lost as electromagnetic radiation because we observed these NSs in the first place. Moreover, in the relatively rare cases where the braking index[63] n can be inferred from the spin evolution, we know that it is not close to the $n = 5$ expected for a NS mountain. This indicates that, while GW losses may contribute, they do not dominate in these systems.

How large should we expect the mountains to be? The size of a NS mountain depends on unknown nuclear physics and the star's evolutionary history. To get an estimate, we focus on the physics of a deformed crust: its shear modulus and breaking strain. An energetics estimate (see e.g. [2931] for details) leads to $\epsilon_{\max} \approx 2 \times 10^{-7}\,(\bar{\sigma}_{\max}/0.1)$, where there is some degree of uncertainty around how large the crustal breaking strain $\bar{\sigma}_{\max}$ may be. Molecular-dynamics simulations for high-pressure Coulomb crystals suggest that the lattice is remarkably strong; $\bar{\sigma}_{\max} \approx 0.1$ [2932]. For comparison, terrestrial solids lie in the range $10^{-4} \leq \bar{\sigma}_{\max} \leq 10^{-2}$. For a NS with radius $R \sim 10$km, this would lead to deformations of the size $\epsilon_{\max} R \sim 0.1$ cm. Going beyond this simple estimate by also considering the stellar interior, the star's relaxed shape, and assuming that the crust is maximally strained at every point [2933] yields an estimate for the maximum allowed ellipticity for a $M = 1.4 M_\odot$ star (with the DH(SLy4) equation of state [2695]) of [2930]

$$\epsilon_{\max} \approx 3 \times 10^{-6} \left(\frac{\bar{\sigma}_{\max}}{0.1} \right). \tag{7.8}$$

The result differs by a factor of a few from the simple energetics argument. However, it was noted in [2934], and later discussed in more detail in [2935], that demanding the crust to be at breaking strain throughout forces the NS into a shape that violates physical boundary conditions. The question then becomes how close a real system can get to this idealized, unphysical state. A useful step towards the answer was taken in [2935], where a fiducial deforming "force" was introduced in the problem (see also [2936]) that contains information about the non-spherical shape of the crust if it were relaxed. This force plays no role in supporting the mountain; the deformed shape of the star is self-consistently supported by crustal strains and represents a solution to the elastic perturbation equations. This approach results in smaller predicted mountains but is closer to realistic evolutionary scenarios and an understanding of how deformations actually arise.

Further work is needed on several fronts in order to make reliable computations of how NS mountains form and which is their typical size. Firstly, going beyond the assumption of a purely elastic crust we probably need to take into account some form of plastic behavior [2937–2939]. In a plastic flow the crust may retain some of the strain beyond the yield point and as a result be able to develop larger quadrupole moments. Secondly, realistic mountain models

[63] The braking index is the exponent of the power law describing the time evolution of the NS spin frequency, $\dot{\nu} \propto -\nu^n$, see section 8 for more details.

JCAP03(2026)081

need to involve evolutionary aspects (some of which will be discussed in section 8) and we may seek guidance from electromagnetic observations, as in the case of the spindown upper limit argument. For example, it has been suggested that the observed population of millisecond pulsars is consistent with a *minimum ellipticity* of $\epsilon \approx 10^{-9}$ [2940].

Accreting NSs have long been considered promising GW emitters [1881, 2941–2943]. Accreting gas is expected to transfer angular momentum to the NS [2944, 2945] and the magnetic field will direct the matter flow towards the star's poles. Assuming the magnetic poles are misaligned with the rotation axis, the star will naturally develop a mass asymmetry. This argument may be somewhat simplistic, but it provides key motivation for detailed studies discussed in section 8. Specifically, ref. [1881] proposed that the observed spin frequencies in low-mass X-ray binaries could be explained by the accreted matter heating the crust giving rise to temperature-sensitive nuclear reactions involving electron captures. Hotter regions of the crust would have these reactions at lower pressures, so the density variations would occur at higher altitudes in these regions. This naturally generates a quadrupole moment, commonly referred to as a *thermal mountain*. There have been further developments of this work, mostly in an effort to provide more detail to the modeling [2933, 2946–2948]. These models require a precise understanding of the composition of the NS crust (see for example [2949]).

The most recent search for continuous GWs from known pulsars using LIGO-Virgo O3 data [2950] pushed the upper limit on the signal strain amplitude below the *spin-down limit* for 23 of the target systems. Among these, the inferred upper limits on the ellipticity for J0437-4715 and J0711-6830 are 8.5×10^{-9} and 5.3×10^{-9}, respectively; only a factor of few larger than estimate from [2940]. Future prospects with ET are summarized in figure 125, which shows the smallest detectable ellipticity for a search over three years (85% duty cycle) with a network of two L-shaped detectors, each with 15 km arms (top plot) or a single triangular detectors, with 10 km arms (bottom plot).

These estimates show that there are hundreds of pulsars for which ET will be able to, if not detect a signal, set constraints below the maximum ellipticity predicted by theory. From the figure, we also see that for tens of high frequency millisecond pulsars, ellipticities below 10^{-9} will be probed. Based on these predictions and the available theoretical results, the detection of at least one continuous GW signal by ET seems likely. What information can be drawn from a detection is not a completely solved problem and is a hot topic in the field [2928]. In particular, we need to better understand systematics and degeneracies, see for example [2951] for a relevant discussion.

For a source with an estimated distance, the measure of the signal amplitude and frequency would provide a measure of the $l = m = 2$ quadrupole moment [2952]

$$Q_{22} = \sqrt{\frac{15}{8\pi}}\, I_{zz}\epsilon. \tag{7.9}$$

This may permit us to exclude EOS models that do not allow quadrupole moments as large as the measured one. Neutron star distance measures typically come from EM observations, like for many known pulsars, but purely GW methods based on the parallax effect have been proposed in [2953, 2954] for EM-silent sources. The results suggest that relative distance errors $\Delta d/d \sim (1-10)\%$ can be obtained with ET over an observation time of 1–3 years, for source distance in the range 0.1–1 kpc and ellipticities in the range $10^{-9} - 10^{-7}$. In general,

JCAP03(2026)081

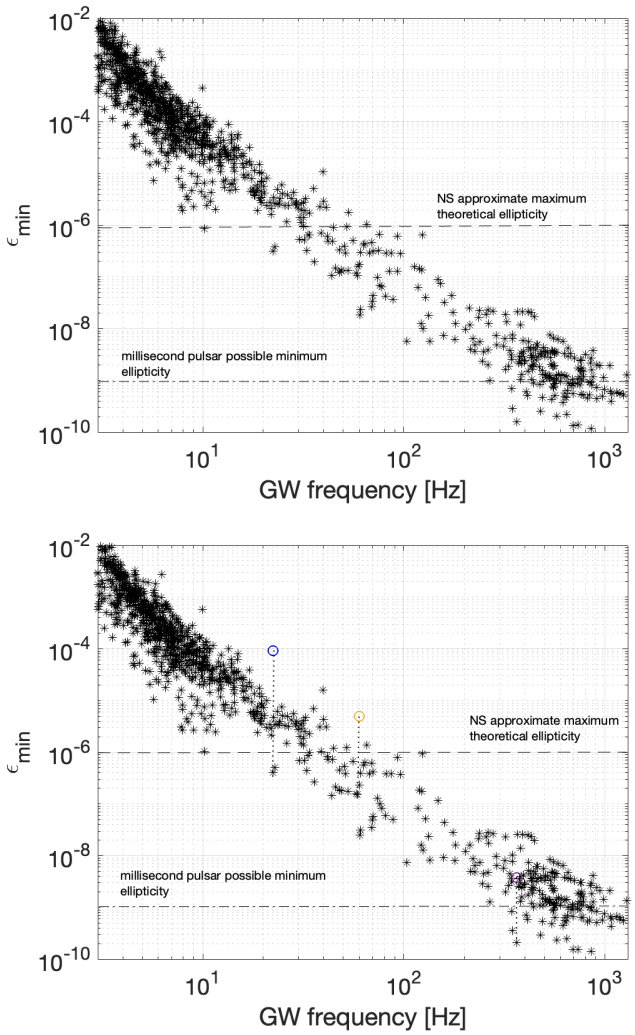

Figure 125. Smallest detectable ellipticity for a search for CWs from known pulsars using a network of two L-shaped ET detectors, with 15 km arms (top plot) or a single triangular detector (bottom plot), with 10 km arms. In both cases, an observation time of three years, with duty cycle 85%, has been considered. The horizontal dashed line roughly indicates NS theoretically predicted maximum ellipticity, see discussion in the main text. The horizontal dashed-dot line indicates a suggested possible minimum ellipticity of observed millisecond pulsars [2940]. For comparison, the three circles indicates upper limits obtained in O3 LIGO-Virgo run for pulsars Vela ($f \simeq 22.38$ Hz), Crab ($f \simeq 59.89$ Hz) and J0711-6830 ($f \simeq 364.23$ Hz).

we expect the distance error to dominate the errors in other GW-derived parameters, like the signal strain amplitude, the frequency, and its derivatives. If the GW contribution to the spin-down is dominant or can be estimated, a measure of the star's moment of inertia, with relative error $\Delta I_{zz}/I_{zz} \approx 10\%$ may be possible [2954]. An independent measure of the star's mass or radius would in any case be necessary to constrain the EOS, see, e.g., [2955–2958]. A quantitative model of how accurately the EOS could be determined assuming the observation of one or more continuous GW signals, possibly in combination with results from EM facilities, remains to be worked out. It is clearly a very important step to be taken.

JCAP03(2026)081

The magnetic field. If we focus on the issue of why mountains form in the first place, then it is natural to consider the star's magnetic field. A dipole magnetic field breaks the (essentially spherical) symmetry of the star, deforms the star [2959], and is expected to lead to some level of GW emission. In fact, the internal magnetic field sets a natural lower limit on NS deformations. However, magnetic fields in NS interiors remain poorly understood. Even for the external field some studies suggest the presence of complex magnetic-field structures beyond the standard dipole assumption; see [2754–2757, 2960, 2961].

For the magnetic field, an argument comparing the energy stored in the magnetic field to the gravitational potential energy leads to [2962]

$$\epsilon \sim \frac{B^2 R^3}{GM^2/R} \approx 10^{-12} \left(\frac{R}{10\,\mathrm{km}}\right)^4 \left(\frac{1.4 M_\odot}{M}\right)^2 \left(\frac{B}{10^{12}\,\mathrm{G}}\right)^2 , \tag{7.10}$$

where B represents the magnetic-field strength. As in the case of the crust, the NS's self-gravity is very strong compared to the magnetic field so the expected deformations are (very) small. However, this estimate of the field strength is based on the *external* magnetic field inferred from pulsar timing. The interior field, which will be more relevant for the shape of the star, is highly uncertain and presents (quite predictably) a complicated problem. The main theoretical challenge is our present inability to construct stable magnetic NS models. Both analytical [2963, 2964] and numerical studies [2965, 2966] indicate that purely poloidal and purely toroidal magnetic fields are unstable on dynamical timescales. Mixed fields, where the toroidal field threads the closed-field-line region of the poloidal component, the so-called twisted-torus configuration, may be stable [2967–2969], but this result appears to be EOS dependent [2970, 2971]. Much of our present understanding involves idealized assumptions such as ideal magnetohydrodynamics and barotropic equations of state. It could also be that a real NS is not always in equilibrium — the magnetic field may be gradually evolving, and this could be important [2972]. Moreover, the high-density NS interior is expected to form a large-scale superconductor [2973]. In that case, estimates suggest that a purely toroidal field leads to the ellipticity scaling as [2974, 2975] $\epsilon \sim 10^{-9}\,(B/(10^{12}\,\mathrm{G}))\,(H_\mathrm{c}/(10^{15}\,\mathrm{G}))$, where H_c is the critical field strength (above which the superconductivity is broken). Again, this estimate is highly uncertain. In principle, a strong magnetic field, like that of a magnetar (of order 10^{15} G), may enable the star to develop a large ellipticity, of order that expected from crust deformations [2725], see section 8 for discussion. This is yet another degeneracy of the continuous GW problem.

The magnetic field also comes into play in accreting systems. In fact, an accreting NS is expected to develop an asymmetry through the magnetic field confining the accreted matter [2976–2984]. Accretion will interact with the magnetic field and compress it, such that there will be locally strong fields on the star's surface. Estimates suggest that this can lead to slightly larger deformations than those sourced by the background magnetic-field configuration, but (again) precise modeling is difficult. The accretion problem will be discussed in more detail in section 8.

Unstable r*-modes.* Neutron stars host a rich spectrum of oscillation modes [2985]. These oscillations are closely connected to the physics of the stars. Essentially, each characteristic of the star, e.g., the density, composition gradients, rotation has a corresponding mode family,

JCAP03(2026)081

e.g., the p-modes, g-modes, inertial modes. The mode properties are intrinsically linked to the properties of the nuclear matter. An excited non-axisymmetric oscillation mode will emit GWs, presenting an opportunity to probe dense nuclear matter through observations. However, the oscillatory motion will be damped by the radiation and viscosity in the stellar fluid (which is sensitive to nuclear transport coefficients) and this damping may be quite rapid. For this reason, it is natural to consider instabilities that cause the oscillations to grow, such as the *Chandrasekhar-Friedman-Schutz (CFS) instability* [2986, 2987].

The CFS instability arises in rotating stars. The idea is as follows: There are two frequencies associated with an oscillation of a spinning star — the frequency as measured by an observer co-rotating with the star and the frequency according to an inertial observer. Suppose the mode is travelling in retrograde to the star's rotation such that the inertial frequency is smaller than the co-rotating frequency. If the star spins fast enough, it will drag the mode along with its rotation such that the inertial observer will see the mode travelling in the prograde direction. The emitted gravitational radiation comes from the non-axisymmetric motion of the star in the inertial frame. The GWs will carry positive angular momentum away from the star, which will be subtracted from the mode. Since this mode is travelling in retrograde in the rotating frame, it carries negative angular momentum and the radiation will cause its amplitude to grow. This, in turn, will increase the amplitude of the radiation, leading to an instability.

Many families of NS oscillation modes contain members that, for sufficiently fast rotation rates, satisfy the CFS instability criterion (for reviews, see [2988, 2989]). The (currently) most promising candidates for the instability are the inertial r-modes [2941, 2990, 2991]. The r-modes are generically unstable in perfect fluids [2992, 2993] because they are retrograde in the rotating frame but prograde to an inertial observer at any rate of rotation.

In reality, NSs are more complex than perfect fluids. Notably, they exhibit viscosity, which damps the fluid motion. To assess the actual relevance of the r-mode instability, one must compare the growth timescale associated with the GW emission with the damping timescales that arise due to, in the first instance, shear and bulk viscosity [2994, 2995]. However, most current estimates of these timescales rely on Newtonian gravity. The relativistic r-mode problem is complicated (and may involve a continuous spectrum [2996, 2997]). Nevertheless, the Newtonian estimates provide important qualitative insights, while we await the developments required to understand the relativistic problem better.

Calculations of the competing timescales demonstrate the existence of an *instability window*. The details depend on the state and composition of the nuclear matter. Broadly, dissipation due to shear viscosity suppresses the r-mode at low temperatures, while the bulk viscosity dominates when the star is hot. There exists critical rotation rates at which each viscosity balances the radiation-reaction growth. The instability window maps out a region of parameter space in temperature and stellar spin, where the r-mode is unstable and will grow. In order to model the associated GW signal, we also need to understand the amplitudes the unstable modes may reach. This is a difficult problem as it requires nonlinear hydrodynamics (the coupling of modes, touching upon turbulence) [2998]. Given our relative ignorance of the nuclear physics and our inability to calculate the relativistic r-modes [2999], we do not have a precise description of the instability window. Neither do we complete understand the

JCAP03(2026)081

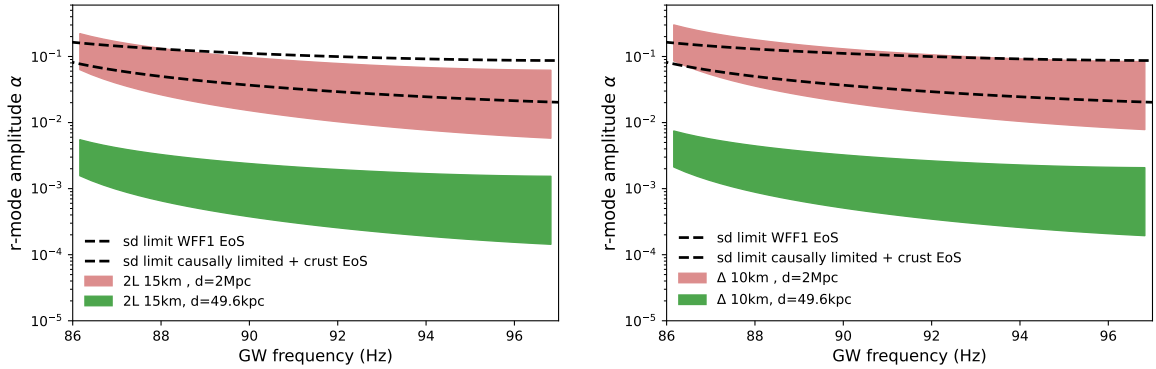

Figure 126. Constraints on the r-mode amplitude α using a network of two L-shaped ET detectors, with 15 km arms (left plot) and the triangle configuration, with 10 km arms (right plot), over three years, assuming in both cases a detector duty cycle of 85%. The considered parameter space corresponds to that of pulsar J0537-6910. The two colored bands corresponds to a range of EOS, from a stiff causally limited EOS with crust [1884] to a soft WFF1 EOS [3002], assuming a distance $d = 49.6$ kpc (green band), which is the distance of pulsar J0537-6910, and a hypothetical source emitting at the same frequency and with distance $d = 2$ Mpc (red band). The two dashed lines define the spin-down limit for the same range of EOS.

nonlinear fluid aspects. Nonetheless, it is possible that r-modes limit the spin frequencies of hot, newly born pulsars [3000, 3001] and more mature accreting systems [1881, 2943].

From an observational point of view, the GW signal emitted by excited r-modes is continuous, with a frequency $\approx (4/3)\nu$, where ν is the star rotation frequency. The precise value of the GW frequency f actually depends on the EOS, and has been parametrized in [3003] (making reasonable assumptions) as

$$f = A\nu - B\left(\frac{\nu}{\nu_K}\right)^2 \nu, \tag{7.11}$$

where ν_K is the Keplerian frequency and the two parameters A, B depend on the EOS. For an astrophysically motivated set of EOS considered in [3003] we have $1.39 < A < 1.57$ and $0 < B < 0.195$. If the GW emission is completely due to r-modes, the corresponding "spin-down limit" strain amplitude is given by

$$h_{\rm sd} = \sqrt{\frac{10GI_{zz}}{c^3}\frac{\nu|\dot{\nu}|}{f^2}}\,\frac{1}{d}\,, \tag{7.12}$$

where d is the source distance. The corresponding r-mode amplitude is

$$\alpha_{sd} = \sqrt{\frac{5}{8\pi}}\frac{c^5}{G}\frac{h_{\rm sd}}{(2\pi f)^3}\frac{d}{MR^3\tilde{J}}\,. \tag{7.13}$$

This quantity, which depends on the EOS through the relation $f(\nu)$, the star's mass and radius values, and the dimensionless canonical angular momentum of the mode, $\tilde{J}$ (which is weakly dependent on the EOS) can be compared to a given search sensitivity, that is to the minimum detectable r-mode amplitude. In case of a detection, parameters A and B of eq. (7.11) could be estimated, constraining the range of possible NS EOS. Even in case of

JCAP03(2026)081

non-detection, setting an upper limit below the spin-down limit allows to constrain the mode amplitude, giving some insight on the excitation mechanism.

A recent search for r-mode emission from pulsar J0537-6910 has been conducted using LVK O3 data [3004]. This is a frequently glitching X-ray pulsar, and the search was motivated by the observation that spin evolution in the inter-glitch period could be driven by r-mode oscillations [3005]. The search set upper limits around or below (depending on the assumed EOS) the spin-down limit over the narrow frequency band 86–97 Hz, beginning to constrain the range of mode amplitudes predicted by theoretical models.

Figure 126 shows the predicted constraints on the r-mode amplitude, α, considering two possible ET configurations, one consisting of two L-shaped ET detectors, each with 15 km arms, and one consisting of a single triangular observatory, with 10 km arms. In both cases, a semi-coherent search over three years (with a detector duty cycle of 85%), with each data segment of duration three months, is considered. Moreover, we assume a search aimed at a source with the same parameters (spin frequency and spin-down) as J0537-6910 at two possible distances, $d = 49.6$ kpc (the distance of J0537-6910) and a hypothetical distance of $d = 2$ Mpc. For each assumed distance we plot constraints corresponding to a range of EOS, going from a causally limited stiff EOS in the core, connected to a crustal EOS [1884], to the observationally motivated soft WFF1 EOS [3002]. These estimates are compared to the range of spin-down values, computed from eq. (7.13) taking $M = 1.4M_{\odot}$, $R = 12$km and $\tilde{J} = 0.0164$, the values for a $n = 1$ polytrope [3006]. For a galactic source like J0537-6910, ET would be able to probe $\alpha \in [10^{-4},\ 10^{-2}]$, possibly allowing us to test various proposed mechanisms for saturating the r-mode instability. A hypothetical source emitting gravitational waves at the spin-down limit, i.e., with $\alpha \approx 10^{-2} - 10^{-1}$, would be detectable at a distance of about 2 Mpc.

7.3.2 Constraints on microphysics at finite temperature

7.3.2.1 Postmerger GWs. In general, for numerous parameter combinations of the individual masses of the stars, BNS mergers will give rise to short-lived or long-lived remnants that could emit a GW signal also after the merger before the collapse to a black hole [3007]. In fact, the post-merger phase is strongly affected by the evolution of nuclear matter at high densities with temperatures reaching values of up to ≈ 100 MeV; therefore, higher densities than during the inspiral and thermal effects in nuclear matter can be tested, see e.g. [3008, 3009] for recent reviews.

In [3010], the authors used numerical-simulations to derive a correlation between the GW frequency in the post-merger phase and the EOS of NS matter. Since then, numerous studies have followed and revealed several possible relations between inspiral and postmerger properties. Specifically, the main characteristic peak in the GW amplitude spectral density was found to be correlated with the radius of the maximum-mass TOV solution or other quantities, such as the tidal deformability of the stars, which are directly accessible through GW observations of the inspiral. The left panel of figure 127 (taken from [3010]) shows the typical GW spectrum one can expect from the post-merger phase of a BNS merger leading to a hypermassive or supramassive NS remnant.

As seen in figure 127, the post-merger signals are emitted at high frequencies ($\approx 2 - 4$ kHz), and therefore, their detection by the current LIGO-Virgo-KAGRA interferometers is

JCAP03(2026)081

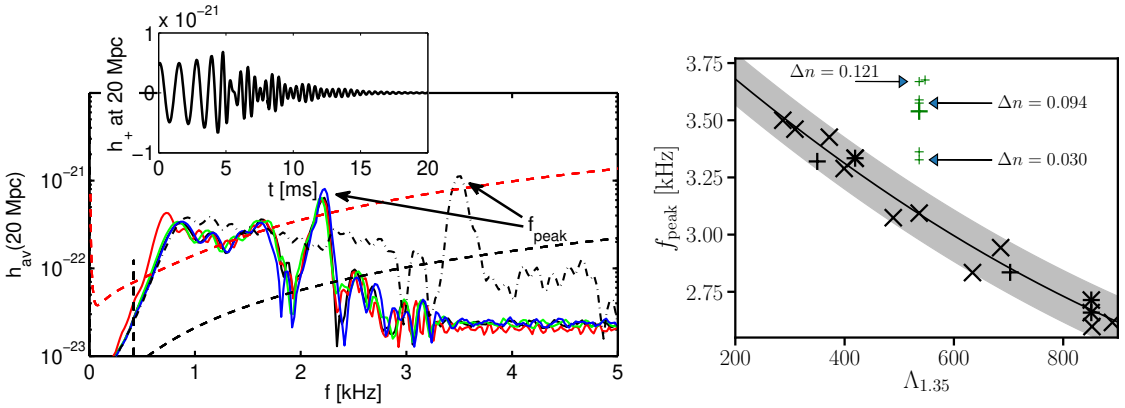

Figure 127. *Left panel:* orientation-averaged spectra of the GW signal for different EOSs and the Adv LIGO (red dashed) and ET (black dashed) sensitivity curves. The inset shows the GW amplitude of the + polarization at a distance of 20 Mpc for one of the EOSs. Reprinted figure with permission from [3010], Copyright (2012) by the American Physical Society. *Right panel:* peak frequency of the postmerger GW emission as a function of tidal deformability Λ for a $1.35M_\odot - 1.35M_\odot$ NS-NS merger. Black symbols are for purely hadronic EOSs, while green symbols are for EOSs which include a phase transition to quark matter; characterized by a density jump Δn given fm^{-3}. The solid curve shows a fit for the purely hadronic EOSs. Reprinted figure with permission from [3011], Copyright (2019) by the American Physical Society.

limited by their sensitivity, and no detection has been reported so far (see [3012, 3013] for a search in the case of GW170817). The higher sensitivity of the ET detector at such high frequency could instead allow for a detection of such signals [3014]. Unfortunately, at the moment, we are still lacking accurate enough approximants that could be used in parameter estimation, but some models have been suggested, e.g., [2467, 3015–3019], as well as agnostic data analysis techniques that could be used without templates, e.g., [3020, 3021]. However, a current issue is that different numerical-relativity codes, even if producing similar results from a qualitative point of view, still produce quantitative differences in the post-merger phase for the same BNS systems [3022]; see section 7.4.2. In the following, we will outline some of the science targets or studies doable with future postmerger detections.

In general, it is also worth highlighting that the use of EOS-insensitive relations (e.g., refs. [409, 2464, 3023, 3024]) allows not only for the reduction of the d.o.f. in waveform modeling and enables Bayesian studies, e.g., [2467, 3017, 3025, 3026], or to search for possible phase transitions, it also helps to perform pre/post-merger consistency tests [3016, 3027]; as described below. However, these relations are always derived based on a selected set of EOSs, which do not cover all possible scenarios, e.g., the presence of phase transition could alter derived relations and leads to systematic biases. This emphasizes the need for further studies in the coming years to ensure that the full potential of postmerger detections is revealed.

Determining NS properties for maximum-mass TOV stars. Post-merger frequencies are expected to reveal information on remnants with up to two times the original component's mass reaching $\sim (3-6)\rho_0$, with ρ_0 denoting as before the nuclear saturation density. For those post-merger remnants that do not promptly collapse into black holes, NR simulations predict loud GW transients with a characteristic main peak frequency. The postmerger main

JCAP03(2026)081

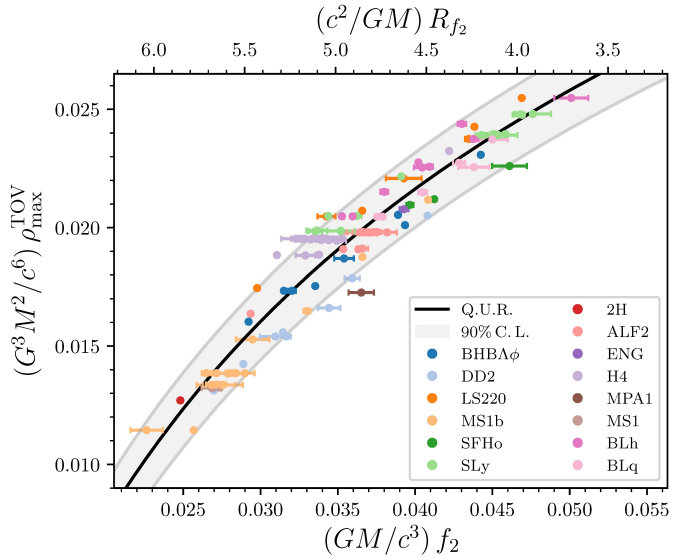

Figure 128. Empirical relation (black line) for the maximum central density $\rho_{\rm max}^{\rm TOV}$ of a non-rotating NS as function of the postmerger peak frequency f_2 and the Keplerian radius R_{f_2}. The colored markers show the data extracted from 289 numerical-relativity simulations with 14 EOSs, whereas the shadowed area indicates the 90% credibility region of the fit. Reprinted figure with permission from [3025], Copyright (2022) by the American Physical Society.

peak frequency f_2 can be phenomenologically associated with an effective remnant radius using Kepler's law [3025]. Even though this quantity has no direct physical interpretation in terms of the remnant properties, it correlates with the maximum central density $\rho_{\rm max}^{\rm TOV}$ of a non-rotating equilibrium NS with a weak dependence on the EOS. This relation $\rho_{\rm max}^{\rm TOV}(R_{f_2})$ is illustrated in figure 128. Hence, to a good approximation, the maximum density $\rho_{\rm max}^{\rm TOV}$ can be inferred from a full-spectrum BNS GW observation, including the postmerger; where some further work is required to robustly check these relation shown in figure 128 in the presence of a strong phase transition and more realistic microphysics. Hence, a postmerger detection can generally impose bounds on the maximum NS mass $M_{\rm max}^{\rm TOV}$ and several postmerger detections could enable a slightly more accurate measurement [3028] complementary to that from an inspiral EOS inference [2460, 3017, 3029, 3030]. The minimum NS radius $R_{\rm max}^{\rm TOV} = R(\rho_{\rm max}^{\rm TOV})$, that is the radius of a NS at maximum density $\rho_{\rm max}^{\rm TOV}$, is crucial information to constrain the mass-radius diagram for NSs. It can be extracted from quasiuniversal relations between the postmerger peak frequency [3028] and measured with an uncertainty of $\sim 2\,$km at postmerger signal-to-noise ratio of 10 [3017, 3031]; see [2466, 2467, 3016, 3032]. It is worth noting that, in the presence of strong phase transitions, and additional physics such as viscosities, the accuracy of the employed quasi-universal relations might decrease, and constraints might be weaker. Imposing stronger constraints on the EOS from BNS mergers will be feasible by combining GW observations with other messengers, e.g., [2342, 3033, 3034].

Search for Phase Transitions and pre/post-merger consistency tests. The higher densities and temperatures produced after merger may also trigger phase transitions. Such phase-transitions can significantly modify the dynamics and hence the GW emission, so that

JCAP03(2026)081

in some cases, the post-merger GW frequency would not match anymore with previously derived predictions [2471, 3011] (e.g., see right panel of figure 127). As mentioned, in the absence of phase transitions, the characteristic post-merger GW frequency can be correlated with the tidal deformability Λ, inferred during the inspiral, e.g., [2464, 2465]. Combining inspiral and post-merger GW detections with ET could therefore allow for the detection of phase transitions (e.g., see [3026]). At the moment, simulations accounting for phase transitions have focused mainly on two possible scenarios: the softening of the EOS due to the appearance of hyperons (e.g., [2477]) and the transition to deconfined quark matter (e.g., [2471, 2472, 3011, 3035, 3036]). It has also been pointed out that unless the phase transition is 'strong', it could be difficult to disentangle the deviations from other uncertainties, e.g. [1234], and the shift in the peak could also be due to non-convex dynamics [3037], both of which are areas for further work. The onset of new d.o.f. such as hyperons and quarks, may also impact viscosities, potentially leading to further shifts of the peak frequency, and manifest in sub-dominant oscillations of post-merger objects, e.g., [2893, 3035, 3038].

Thermal Effects. Due to the high temperatures reached after the merger, thermal effects in the EOS impact the GW emission in the post-merger and hence become detectable by ET [2479, 3039–3041]. Different studies have demonstrated that they alter the GW spectrum and shift the dominant post-merger frequency by amounts ranging from 60 to 200 Hz, depending on the underlying EOS [3042]. Hence, future detections with ET allowing precise measurements of the cold part of the EOS during the inspiral could be complemented by post-merger observations to infer the thermal properties of the EOS [2479, 3043]. However, to enable extracting accurate information about the finite temperature EOS requires further work on analyzing quasi-universal relations and other observables in settings that go beyond the approximate treatment of thermal effects within the EOS often used in current studies, which requires a large community effort due to the complexity and computational costs of numerical-relativity simulations.

Influence of Magnetic Fields. Another possibly important effect is due to the very large magnetic fields that may be formed after merger [3044–3047]. In this case, while many simulations suggest that the post-merger GW frequency should not be significantly affected [3034, 3048, 3049], unless large magnetic field strengths are present before the merger [3050, 3051], others claim that the GW amplitude and luminosity may be suppressed [3052], making a detection more difficult, or that the frequency shift of the post-merger signal could be high enough to mask effects due to phase transitions in the EOS [3051]. This is because magnetic turbulence acts as an effective viscosity on the fluid, redistributes angular momentum, and may accelerates collapse to BH.

Inference of prompt black-hole formation. Constraints on the EOS may also be provided by inferring the threshold binary mass for prompt black-hole formation in NS mergers from analyzing the GW signal radiated in the inspiral phase. The merging of two NSs may lead to either the formation of a BH or of a NS remnant [2469, 3053]. A direct gravitational collapse occurs if the binary's total mass $M_{\rm tot}$ is higher than some threshold mass $M_{\rm thres}$ beyond which the forming remnant cannot be stabilized. For lower $M_{\rm tot}$, rapid differential

JCAP03(2026)081

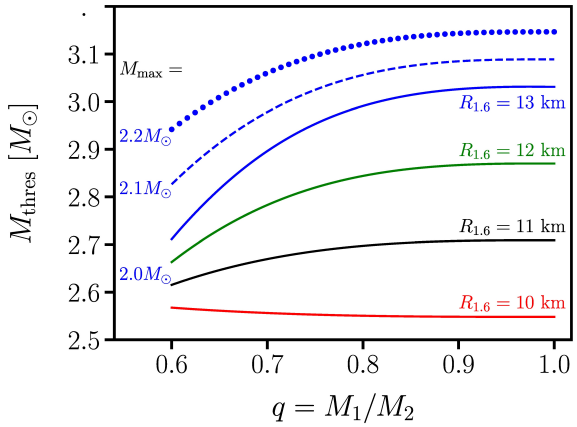

Figure 129. Threshold binary mass for prompt collapse as a function of mass ratio for different neutron star radii. Solid curves assume a fixed maximum mass of $M_{\rm max} = 2M_\odot$ but different NS radii. Blue curves show $M_{\rm thres}(q)$ for a fixed radius $R_{1.6} = 13\,$km but with $M_{\rm max}$ being $2.0M_\odot$ (solid), $2.1M_\odot$ (dashed) and $2.2M_\odot$ (dotted). Figure adapted from ref. [2915]. Reprinted figure with permission from [2915], Copyright (2021) by the American Physical Society.

rotation and thermal pressure support the central object against prompt collapse even if $M_{\rm tot}$ is larger than the maximum mass of non-rotating NSs. Such systems may undergo a delayed collapse to a BH due to the reduction of angular momentum and cooling [2915]. The merger outcome is predominantly determined by the ratio of the total mass $M_{\rm tot}$ and the threshold mass $M_{\rm thres}$ [3054, 3055]. The system with the lowest $M_{\rm tot}$ and observational indications for a prompt collapse gives an upper limit on $M_{\rm thres}$, whereas a detection with characteristics excluding a prompt collapse limits $M_{\rm thres}$ from below. In general, the dynamics of NS mergers depend on the incompletely known EOS of high-density matter [1815, 2654] and other parameters such as the mass ratio or the spin of the merging stars [3056, 3057]. Over the last years, numerous phenomenological relations for $M_{\rm thres}$ have been derived, e.g., [2915, 3055, 3057–3059]. figure 129 shows one such relation, where the threshold mass is lined to the mass ratio and the typical radius of a NS with a mass of $1.6M_\odot$, $R_{1.6}$. However, further work is needed to verify the robustness of the relations, for example, ref. [3060] finds that the threshold mass does not have a universal behavior under EOS variations for $q \neq 1$ as the collapse is induced by the tidal disruption and accretion of the secondary star [3009, 3061, 3062]. However, [3060] demonstrate that observations of prompt collapse thresholds, either from binaries with two different mass ratios or with one mass ratio but combined with the knowledge of the maximum NS mass or compactness, will constrain the incompressibility at the maximum NS density $K_{\rm max}$ to within tens of percent. Hence, measuring the maximum mass in combination with the other systems' parameters directly helps us to constrain important information about the EOS.

Accuracy in the measurement of postmerger properties. Recent investigations have attempted to estimate the accuracy with which the post-merger signal could be measured by next-generation GW observatories. For example, in [3063] the authors estimated an error in the measure of $f_{\rm peak}$ (sometimes also referred to as f_2) of $\delta f_{\rm peak} \approx 139\,$Hz at a horizon distance

JCAP03(2026)081

$d_{\rm hor} \approx 267$ Mpc for ET (corresponding to a source with a signal-to-noise ratio of 5 in the post-merger). The same error could be achieved by Advanced LIGO at $d_{\rm hor} \approx 30$ Mpc. The detection rate for the post-merger signal was estimated to be ≈ 1 every 100 years for Advanced LIGO and ≈ 3 per year for ET. Combining the merger and post-merger signal, ET could also detect phase transitions in the post-merger, assuming the phase transition causes a shift in the $f_{\rm peak}$ predicted from the inspiral measured Λ (solid line in right panel of figure 127) of at least 455 Hz (assuming a signal-to-noise ratio of at least 10 in the post-merger [1234]). Due to the limited number of post-merger detections per year, it will probably be necessary to stack multiple detections together in order to increase the accuracy in the determination of the post-merger EOS. One year of observations may indeed not be enough to distinguish between different EOSs in the post-merger phase [3064]. For example, in [3065] it was investigated the possibility of using both power and coherent mode stacking methods and it showed that it could be possible to measure the post-merger frequency and the NS radius with an accuracy of $\approx 4\%$ or better (depending on the EOS) when combing together 30 post-merger detections (i.e., with an error of ≈ 20 Hz on the post-merger peak frequency and less than ≈ 100 m in the NS radius). Such an accuracy should be sufficient to detect phase transition in the post-merger phase, since it may be able to show a difference between the measured post-merger frequency and the one expected from the EOS measured during the inspiral. We need to make clear that studies are still very limited at the moment, since the larger sensitivity of ET in the post-merger phase will require more accurate theoretical predictions. NR simulations, for example, sometimes employ approximate modeling of finite temperature effects instead of a fully tabulated finite temperature EOS (which is more computationally expensive). While current detectors are not sensitive enough to be impacted by such approximations, ET could be affected for sources up to ≈ 44 Mpc in case of softer EOSs, and up to ≈ 113 Mpc for stiffer EOSs [3040] (see also [3041, 3066]).

7.3.2.2 GWs from core-collapse supernovae and proto-neutron stars. CCSN probe the EOS of supranuclear-dense matter in complementary regimes of temperature and density to BNS mergers. CCSNs are triggered when exothermic nuclear burning ceases at the center of a star with a mass between $8M_\odot$ and $100M_\odot$. At this time, the hydrostatic equilibrium is lost and the core (iron) begins to collapse from its original radius of a few thousands of km. The collapse of the core continues until it reaches nuclear densities, at which point the repulsive forces between nucleons cause the collapse to decelerate rapidly. This results in a partial rebound of the inner core, known as the core bounce, which generates a shock wave that propagates outward. The collapse is then halted at the formation of a PNS. At an initial mass and radius of $M_{\rm PNS} \sim 0.6M_\odot$ and $R_{\rm PNS} \sim 50$ km, this object has a moderately relativistic gravitational field, which gets stronger when the newly formed PNS accretes additional matter and contracts.

During this phase, processes such as convection, rotation, and magnetic field interactions, generate non-spherical flows in the core that could produce gravitational radiation. These flows also contribute to all of the mechanisms that have been proposed to initiate a CCSN explosion after the prompt shock has failed to break out of the core. In most stars, they support neutrino-driven explosions by enhancing the efficiency with which neutrinos transport energy from the PNS to its surrounding layers [3067–3069]. In a subset of cores, high rotational and

JCAP03(2026)081

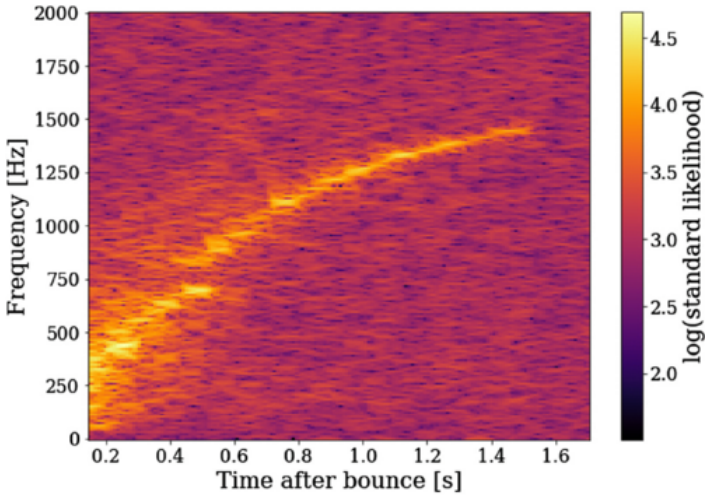

Figure 130. Time-frequency map of the GW signal of a three-dimensional model of the collapse of a star with $20\,M_\odot$ showing a PNS oscillation mode whose frequency rises continuously from the time of core bounce ($t = 0$). Reprinted figure with permission from [3087], Copyright (2023) by the American Physical Society.

magnetic energies drive the explosion in a predominantly anisotropic geometry [3070, 3071]. Even if none of these mechanisms succeeds at launching a CCSN and instead accretion causes the PNS to collapse to a black hole (BH), spherical symmetry will be broken to a considerable degree [3072, 3073]. The GW signal is determined by the dynamic processes in the collapsing core and PNS, exhibiting a range of features with varying amplitudes and frequencies that are sensitive to the stochastic source dynamics and the EOS of nuclear matter.

Information on the EOS in the signal comes from hydrodynamic oscillation modes of the PNS whose frequencies have a direct relation with the structure of the PNS, in particular its mass and radius. The time evolution of the mode spectrum would yield valuable insights into the EOS through GW asteroseismology of PNSs. No such detection has been achieved so far, but progress in theoretical modeling along two lines of work has laid the ground for future observations. As the relevant PNS oscillations are relatively weak perturbations of a slowly varying object close to equilibrium, they can be described as solutions of the linearized hydrodynamic equations [3074–3077]. This approach is computationally inexpensive and thus well suited to scanning the large parameter space of nuclear and stellar physics. It cannot, however, account for the large-scale dynamics of the core, including, e.g., the development of a CCSN explosion, the rate at which mass is accreted onto the PNS, its internal dynamics such as convection, and it cannot predict how and to which amplitude the possible modes are excited. These questions can be addressed by large-scale, multi-dimensional simulations of the entire core that capture (magneto-)hydrodynamics, relativistic gravity, neutrino transport, and nuclear reactions. Such models produce detailed synthetic GW signals but can be very expensive. Thus, only a limited number of them are available [3078–3086]. Figure 130 shows an example result of three-dimensional simulation as a time-frequency map of the GW signal from a $20\,M_\odot$ star. The figure depicts the continuous rise of the PNS oscillation mode frequency starting from core bounce ($t = 0$).

JCAP03(2026)081

Perturbation analyses aimed at uncovering the relationship between GW emission and the physical parameters of progenitors during PNS formation and evolution have shown that the time-frequency evolution of the primary emission mode corresponding to the g-mode or f-mode, closely relates PNS properties such as surface gravity and average density [3088]. Additionally, advanced numerical simulations of CCSN have established empirical relationships that link oscillation modes to intrinsic system attributes and are largely independent of the EOS or progenitor mass [3088]. However, factors like progenitor mass and the EOS for dense matter can influence GW signals, leading to further empirical relationships between the supernova GW frequency and the average density of the PNS [3076]. While most of these relationships are largely EOS-independent, certain PNS g-modes, especially those with decreasing frequencies over time, exhibit a clear EOS dependence [3089]. Building on these insights, a recent investigation has compiled a comprehensive dataset of over 1000 exploding CCSNe models spanning various progenitor masses, metallicities, and nuclear EOS [3090]. This work identified two main frequencies in a range of order 1 kHz, with the lower/higher one associated to the early/late stage of the signal that are sensitive to the EOS, and with the latter being correlated with the surface gravity of the remnant.

Although the frequency range of GW emissions from CCSNe is within the reach of current detectors, the detection range for slowly or non-rotating CCSNe is limited to approximately 5 kpc [2214, 3091]. If the progenitor core exhibits very rapid rotation, as seen in only 1% of electromagnetically observed events [3092, 3093], the distance increases up to 50 kpc. The estimated occurrence rate for CCSNe within the Milky Way is about 1 to 2 per century [3094], making detection challenging for current detectors. For ET, the anticipated event rate is about 0.5 events per year [3095], with a detection range extending up to (2–4) Mpc for neutrino driven explosion and up to (5–30) Mpc for rapidly rotating progenitors [3096]. For a detailed assessment of the observed and expected rates of CCSNe in the local Universe and the Milky Way, see section 8.2.5.

In the case of QCD phase transitions, the GW emission due to the sudden contraction of the PNS results in an abrupt rise in the amplitude by more than a factor of 10, followed by a model-dependent ring-down phase that can last for several hundreds of milliseconds. This unique GW emission, as illustrated in figure 131 (right panel), makes the QCD-driven supernova scenario well distinguishable from a canonical neutrino-driven supernova explosion (see the characteristic GW strain $h_{\rm char}$ in figure 132, comparing S11.2 and S50). The detailed GW analysis of these models demonstrates great potential for their detection in galactic events, with characteristic GW spectral amplitudes more than an order of magnitude above those of normal supernovae in the frequency range above about 1 kHz.

Associated with the GW signal from the QCD phase transition is the emission of a non-standard neutrino burst, dominated by $\bar{\nu}_e$ and contains information about bulk properties of the EOS [3098]. Despite the present uncertainties due to yet-incompletely understood neutrino flavour evolution, this non-standard $\bar{\nu}_e$ burst is detectable at the currently operating generation of water-Cherenkov detectors [3099, 3100]. Such QCD-driven massive star explosions also feature r-process nucleosynthesis [3100].

JCAP03(2026)081

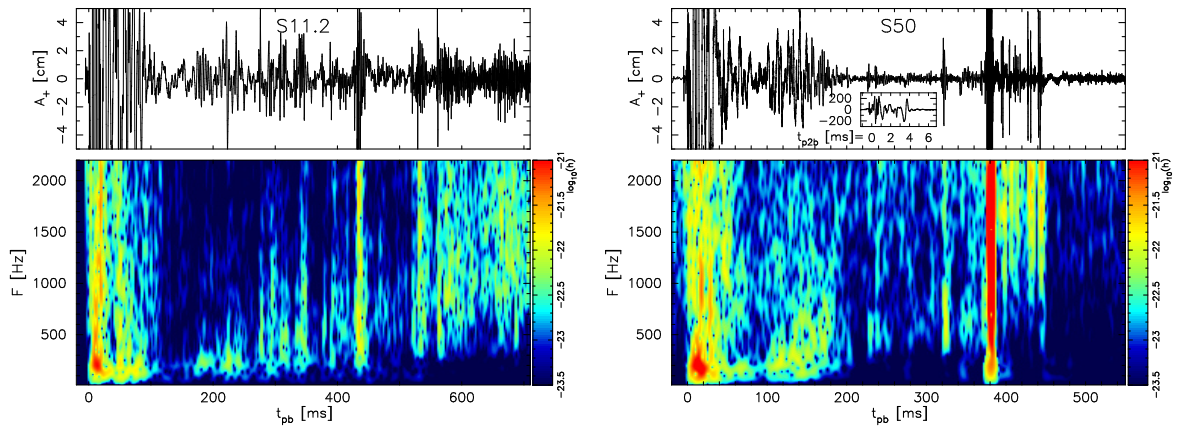

Figure 131. Post-bounce evolution of the gravitational waveform A_+ (top panels) and the corresponding spectrogram (bottom panels) for two representative models, neutrino-driven supernova explosion of a 11.2 $M_\odot$ progenitor model (S11.2) and 50 $M_\odot$ model (S50), the latter featuring a QCD phase transition and associated supernova explosion onset at around 376 ms post bounce, which is accompanied by a sudden rise of the GW amplitude. For S50, a magnified view of the gravitational waveform is shown in the inlay of the top panel with respect to the second bounce time, $t_{\rm p2b}$. Reproduced from [3097]. The Author(s). CC BY 4.0.

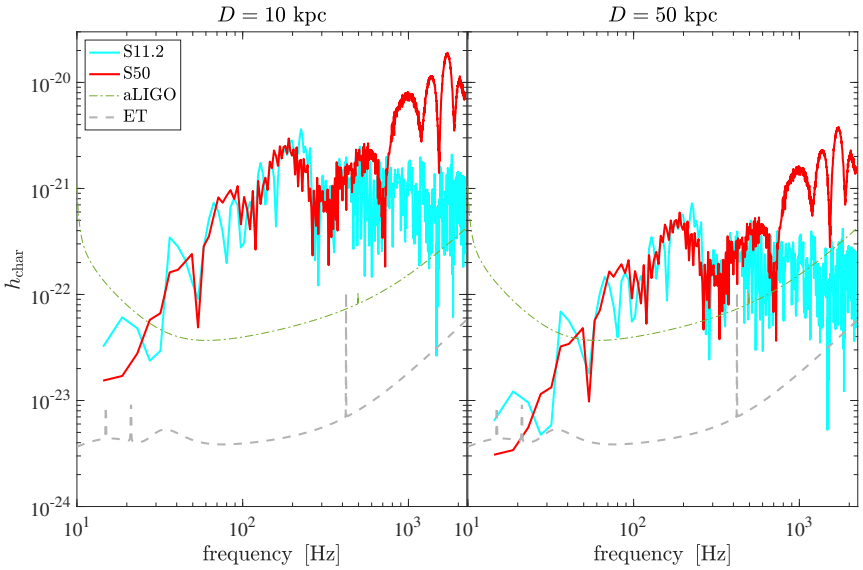

Figure 132. Characteristic GW spectral amplitudes, $h_{\rm char}$, for the two models S11.2 (light blue solid lines) and S50 (red solid lines) shown in figure 131, assuming a source distance of 10 kpc (left panel) and 50 kpc (right panel). The noise amplitudes of aLIGO (green dashed lines) and ET (grey dashed lines) are plotted as references. Figure reproduced based on data from ref. [3097].

JCAP03(2026)081

7.3.3 Nucleosynthesis and multi-messenger signals

In addition to being primary targets for ET, compact binary mergers and CCSNe are key players in galactic chemical evolution, see, e.g., [2843, 3101–3103]. Moreover, the variety of scales and processes involved in these events produce radiation of different kinds, qualifying them as genuinely multimessenger events. In the strong field regime, the heating of dense matter boosts weak reactions and produces intense neutrino radiation (with peak luminosities $\sim 10^{53}$erg s^{-1}) in all neutrino flavors, lasting for seconds and influencing the ejecta composition, see, e.g., [2828, 3104–3106]. At the same time, several mechanisms involving strong magnetic fields, neutrinos, and dynamical spacetime can produce a relativistic jet that drills inside the ejecta or through stellar layers, and possibly breaks out. Once ejected matter has expanded, it becomes transparent enough to emit electromagnetic (EM) radiation over the entire spectrum. In particular, the jet is expected to produce the non-thermal emissions powering the prompt and afterglow emission of gamma-ray bursts (GRBs). According to the present paradigm, compact binary mergers produce short GRBs, while the long ones are produced by the core-collapse of fast rotating, highly magnetized stellar cores (collapsars). Within the same scenarios, the decay of freshly synthesised radioactive nuclei powers the light curves and spectra that characterizes CCSNe and kilonovae.

Nuclear physics represents a key ingredient for the prediction and interpretation of the multimessenger signals from CCSNe and compact binary mergers, as well as of their nucleosynthesis signature. With its unprecedented sensitivity and sky localization capability (especially, if part of a larger network of detectors, not only for GWs, but also for EM radiation and neutrinos) ET will enable us to maximize the outcome of joint multimessenger analysis, see also section 6 and section 8. In particular, it will directly connect the strong field dynamics, where the properties of dense nuclear matter are at play and shape the GW and neutrino signals, with its imprint in post-explosion/post-merger observables, including the EM emissions, as well as the nucleosynthesis yields.

7.3.3.1 Nucleosynthesis in Core-Collapse Supernovae and the r-process. The general picture of nucleosynthesis in standard CCSNe is nowadays well-established [1592]. Extensive calculations were usually performed by means of parameterized spherically symmetric models, e.g., [1759, 3110], including also the study of correlations with the EOS of dense matter [3111]. Three-dimensional models featuring nucleosynthesis calculations have also become available [3112–3115]. Their outcome was compared with observations from CCSN remnants and elemental abundances in the Solar System, in the interstellar medium and in stars of our Galaxy, as well as of nearby galaxies. The largest uncertainties still concern iron-group and heavy element formation in the innermost ejecta, mostly powering the EM luminosity ($\sim 10^{41-42}$ erg s^{-1}). The silicon shell of the progenitor star is expected to experience explosive Si-burning that has ^{56}Ni as the major product. Ejecta coming from deeper layers first photodissociate into neutrons, protons, and α-particles, while the build-up of heavier nuclei occurs during the subsequent expansion. The nucleosynthesis outcome depends mostly on the entropy and on the initial relative abundance of free neutrons and protons (quantified by the electron fraction, Y_e) [3116]. For $Y_e \sim 0.5$, the production of iron-group nuclei can occur. The production of heavy elements beyond the iron-group follows a different path,

JCAP03(2026)081

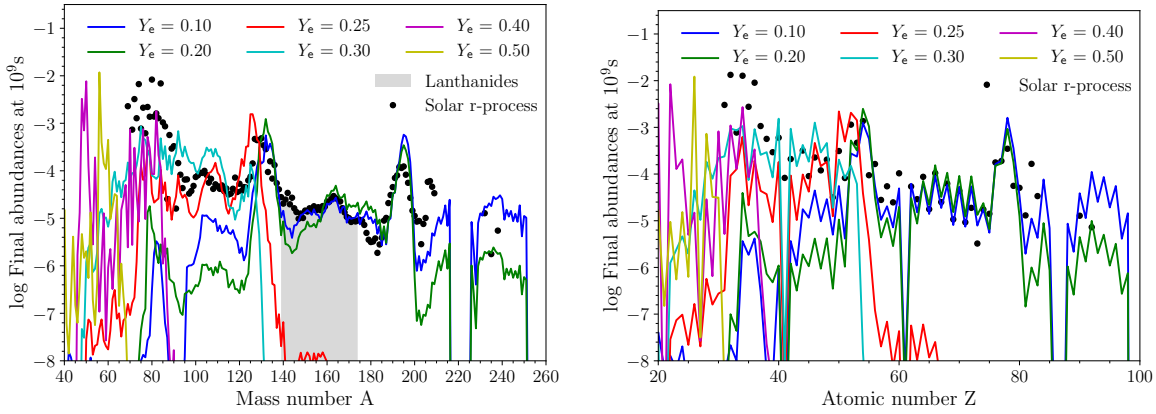

Figure 133. Abundances obtained for a fluid element of entropy $s \approx 10 k_B$ baryon^{-1}, expansion timescale $\tau \approx 10$ ms and for different initial Y_e are presented as a function of the mass number A (left) and of the atomic number Z (right). For $Y_e \lesssim 0.25$, r-process nucleosynthesis produces all heavy elements between the second (Te-I-Xe region) and third (Ir-Pt-Au region) r-process peaks, including lanthanides [3107]. If $Y_e \lesssim 0.15$, also actinides are produced [3107, 3108]. The production of elements between the first (Se-Br-Kr region) and the second r-process peaks requires $0.25 \lesssim Y_e \lesssim 0.4$. Reproduced from [3109], with permission from Springer Nature.

called rapid neutron capture process (r-process) nucleosynthesis, which requires the presence of neutron rich conditions ($Y_e < 0.5$), see e.g. [2843, 3109]. Figure 133 shows the abundances obtained for a representative low entropy fluid element ($s \sim 10\, k_B$ baryon^{-1}) and for different initial Y_e. For low entropy material, matter with $Y_e \gtrsim 0.4$ produces iron-group nuclei and only weak r-process elements. However, in the case of high entropy material ($s \gtrsim 100\, k_B$ baryon^{-1}), an α-rich freeze-out occurs and, even for marginally neutron-rich conditions ($Y_e \lesssim 0.5$), the synthesis of heavy elements proceeds due to the capture of free neutrons on the few available seed nuclei. The electron fraction is set by the interaction between neutrinos and matter. The initial neutrino burst is emitted a few milliseconds after core bounce and followed by accretion-powered thermal neutrino emission characterized by a luminosity $L_\nu \sim 10^{52-53}$ erg s^{-1} and mean energies $\langle E_\nu \rangle$ ~10–20 MeV, with heavy flavor neutrinos hotter than electron ones, due to their deeper decoupling from matter, see e.g. [3117]. In the case of a successful explosion, the neutrino luminosities decrease exponentially over the neutrino diffusion timescale in the subsequent PNS cooling phase. At the same time, the mean energies decrease down to a few MeV and equalize due to the different neutrinospheres approaching each other as the PNS contracts [3118, 3119]. In the context of neutrino-delayed explosion mechanism, neutrinos emitted by the new born PNS interact with matter just behind the shock through reactions like $p + \bar{\nu}_e \rightarrow n + e^+$ and $n + \nu_e \rightarrow p + e^-$. The precise balance between these reactions determines the equilibrium Y_e in the innermost ejecta, e.g., [3120–3123].

The initial entropy, expansion timescale and Y_e are ultimately related to the explosion dynamics (i.e., the explosion mechanism and the shock strength) and to the neutrino luminosities. High-entropy neutrino-driven winds from the nascent PNS were long considered promising r-process nucleosynthesis sites [3116]. However, recent simulations showed that the ejecta of standard CCSNe are not neutron-rich enough to produce robust and strong r-process

JCAP03(2026)081

nucleosynthesis [2810, 2817, 3124]. Only a partial and weak r-process can be realized in some classes of CCSNe, e.g. electron-capture SNe and CCSNe near the low-mass end [3125]. At the same time, the lightest heavy elements, including Sr, Y, Zr, could be produced in neutrino-driven winds [3126], depending on the nuclear physics input, see also section 7.2.3.2. Another argument against the occurrence of full r-process nucleosynthesis in standard CCSNe is the fact that at low-metallicity the abundance of r-process elements is characterized by a large scatter. The latter points to their production in relatively large amounts, but in rare events [3127]. On the other hand, special classes of rare SNe, such as magneto-rotationally driven supernovae [3128–3130] or collapsar [2253, 3131], may harbor suitable conditions in their innermost ejecta to provide strong r-process nucleosynthesis yields. Their existence is, however, still debated, as well as their viability as r-process nucleosynthesis sites, together with their dependence on relevant stellar parameters, such as metallicity, rotational velocity and core inhomogeneities.

The detection of GWs from nearby CCSNe and from long GRBs by ET, especially if combined with the multi-messenger detection of line elements in EM spectra or of thermal neutrinos from the exploding core (see below), could improve our understanding of the nucleosynthesis in the innermost ejecta, mostly by shedding light on the explosion mechanism. In the case of a nearby long GRB, the detection of EM signatures from r-process elements in the associated SN could provide a smoking gun evidence for the existence of rare classes of SNe contributing to r-process nucleosynthesis. In the case of an extremely close (yet unlikely) event ($\lesssim$ a few Mpc), the coincident detection of GWs, more plausible in the case of strong asymmetries in the central engine, could better clarify the nature of the progenitor. Such a discovery would release some of the present tensions in galactic chemical evolution, e.g. [3132].

7.3.3.2 Multimessenger detections of core-collapse Supernovae. In the case of a Galactic CCSN, whose rate is expected to be between 1–2 per century, a multimessenger detection could involve GWs, neutrinos and EM radiation. With optimal GW filters and for cases involving strong asymmetries, the ET detection horizon could reach up 30–500 kpc, i.e., comparable or even larger than the distance of the Large Magellanic Cloud (50kpc) [3135]. The sensitivity of next-generation GW observatories such as ET will be necessary to distinguish between standing accretion shock instability (SASI) and convection-induced modulations in detected GW signals [2214], see also section 7.3.2.2. For a galactic event, future neutrino detectors such as Hyper-Kamiokande, DUNE or JUNO, will detect almost one hundred thousand neutrinos within a few seconds, allowing to investigate in great detail the thermal neutrino emission. Even pre-collapse neutrinos could be observed for a few seconds, probing the latest stellar evolution phases. However, even for a Galactic CCSN, it is not obvious that all three radiation types could be easily detected: while the EM emission could be observable up to redshift $z \sim 1$, if the explosion happens in the Galactic plane and on the other side of the Galaxy, its EM emission will be likely obscured by dust. On the other hand, GWs and neutrinos are largely unaffected by absorption processes within the Galaxy, and their combination can very precisely indicate the time of the explosion and its sky localization [3135–3137]. Moreover, if a massive progenitor star directly collapses into black holes without bright explosion, a failed SN occurs. Such a SN will have a very faint EM signature [3138], while it could have significant GW and neutrino emissions. By measuring

JCAP03(2026)081

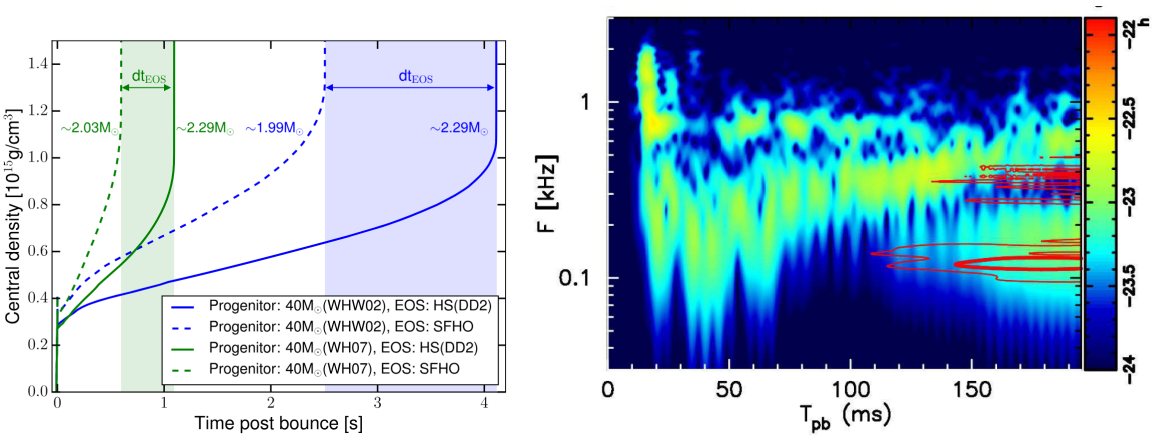

Figure 134. *Left:* evolution of the maximum density in CCSNe producing a BH. For a given progenitor, the nuclear EOS affects significantly the collapse timescale. *Right:* color-coded GW spectrum from a $15M_\odot$ CCSN simulation using the SFHx EOS. The red curves are contours (only for post-bounce times larger than 100 ms) of the $\bar{\nu}_e$'s spectra. The observer's direction is fixed along the z-axis for a source at a distance of $d = 10$ kpc. The overlap observed for this model between the two spectra is evident. Figures reproduced from [3133]. © 2018. The American Astronomical Society. All rights reserved (left) and reproduced from [3134].© 2017. The American Astronomical Society. CC BY 3.0 (right).

the neutrino and GW emission during the first few seconds, a sharp end in both emissions should indicate the time of BH collapse, a feature which is possibly distinguishable from the drop in the neutrino emission due to the explosion. The collapse timescale, in combination with information on the progenitor structure, can set constraints on the EOS of nuclear matter, since the latter sets the density at which the collapse occurs [3133], as visible in the left panel of figure 134. Additionally, the detection and very precise localization of CCSNe in GWs and neutrinos, but very faint in EM radiation, can help mitigate the apparent lack of SNe from stars with initial masses $\gtrsim 17M_\odot$, known as 'red supergiant problem' [3139].

The nuclear EOS and several related quantities, including the symmetry energy, its slope and the nuclear incompressibility at saturation density, can significantly affect the GW [3140–3142], neutrino [3143–3147] and EM emissions from CCSNe through the explosion dynamics and the PNS evolution. For example, a softer EOS is expected to produce a more compact and faster contracting PNS, increasing both the neutrino luminosities and mean energies, as well as the GW frequency and its evolution rate. Additionally, the progenitor variety (e.g., mass, rotation, magnetic field) is expected to produce an intrinsic variability in all emissions, see e.g. [1743, 3069, 3148]. Thus, relevant constraints on nuclear physics require a robust way to disentangle the dependence on the progenitor from the one on the nuclear physics, also breaking possible degeneracies. A multimessenger detection of GWs and neutrinos could help to achieve this, for instance, through correlations between the two types of emission, which are also related to the progenitor mass and compactness, remnant mass and explosion energy [2903]. Moreover, the presence of SASI is expected to induce modulations both in the neutrino and GW signals, as visible the right panel of figure 134, while in the case of explosions dominated by neutrino-driven convection, such a correlation

JCAP03(2026)081

could be barely seen [3134]. Since strong SASI activity is observed in the case of more compact stellar cores, such a detection could favor softer nuclear EOSs. In the case of rapidly collapsing cores, the gravitational collapse can lead to the onset of the low T/W instability within the PNS [3149], also producing correlated signatures in both the GW and neutrino emissions [3150]. The strength and configuration of the magnetic field could also influence the T/W-related emissions as well as their multimessenger detection prospects [3151].

In the case of extra-galactic CCSNe, GW detections by ET could reach such horizons only if strong axisymmetric instabilities are present, for example when the remnant is a BH surrounded by a very massive accretion disk. The joint detection of high energy photons, neutrinos and GWs from a nearby long GRB could help discriminate between different central engines, e.g. an accreting BH from a magnetar, and could set constraints on the nuclear EOS through inference of the maximum NS mass. While ET is expected to boost horizon and sensitivity with respect to current detectors, the observational prospects will however be small, since even for an optimistic GW horizon at the edge of the Local Group ($\lesssim 3$Mpc), the expected detection rate is of the order of a few every 10^5 years due to the low long GRB explosion rate in the local universe [3152]. Only in very optimistic scenarios could ET be able to provide a multimessenger detection within the Virgo Cluster (i.e., ~ 16 Mpc) in the time-frame of several years [3153]. Recently, other possible multimessenger signatures related to collapsar and long GRBs were explored. These include the GW and EM signature produced by the collapse of a very massive He core (above the pair-instability mass gap), possibly also ejecting r-process elements. In this scenario, ET could be able to detect multiband GWs of 0.1–50 Hz from non-axisymmetric instabilities in self-gravitating massive collapsar disks out to hundreds of Mpc [3154]. The resulting EM transient would include a long GRB and a quasi-thermal emission, with intermediate properties between a kilonova and a supernova, and r-process signatures. Another scenario related to CCSNe and long GRBs involves a choked jet, where the relativistic jet fails to break through the stellar envelope, driving a quasi-spherical shock into the surrounding circumstellar material. In this case, high-energy neutrinos are expected to be produced over broader angles compared to a successful jet enhancing the chances of observing both GWs and high-energy neutrinos from nearby Type II CCSNe, which could also be associated with low-luminosity GRBs [3155–3159].

7.3.3.3 Ejecta, nucleosynthesis and kilonova emission from compact binary mergers. Compact binary mergers involving at least one NS have been long considered promising r-process nucleosynthesis sites [3104, 3160, 3161]. Thermal neutrino emission from them shares many similarities with the one of CCSNe. This is due to the similar conditions of matter inside a PNS and in a merger remnant, with possibly larger temperatures and higher densities in the case of BNS mergers [2478]. Additionally, accretion of matter from the disk or torus around the central object provides accretion-powered neutrino luminosity. This becomes the main source of neutrinos in the case of NS-BH mergers or for BNS merger whose remnant has collapsed to a BH. While the mean neutrino energies are comparable to the ones observed in CCSNe, the neutrino luminosities are possibly larger at peak. A valuable difference is represented by the initial dominance of $\bar{\nu}_e$ over ν_e, due to the tendency of cold β-equilibrated matter to leptonize, once decompressed and heated, see e.g., [3162].

JCAP03(2026)081

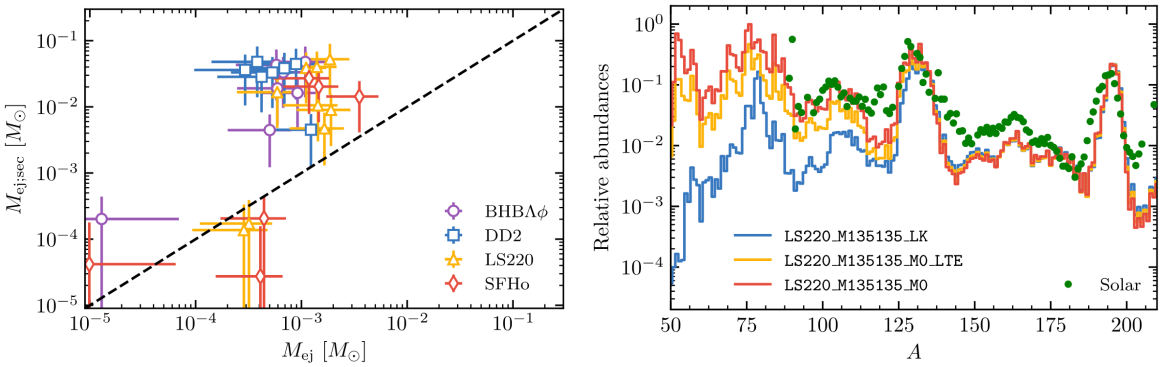

Figure 135. *Left:* dynamical ejecta mass (x axis) VS. secular ejecta mass (y-axis, estimated as 20% of the disk mass) extracted from a large set of BNS merger simulations. Secular ejecta are dominant over the dynamical ones. Different colors show the impact of the nuclear EOS. *Right:* r-process nucleosynthesis from different simulations of the same BNS merger. Simulations featuring neutrino absorption in optically thin conditions (red and orange lines) produce all r-process nuclei, while the simulation not including it (blue line) only strong r-process nucleosynthesis. Reproduced from [2337].

Extensive simulation campaigns showed that different ejection mechanisms and neutrino irradiation operate on different timescales, contributing with different components to the total ejecta [3009, 3163], as visible in the left panel of figure 135. During merger, a mass $\sim 10^{-4} - 10^{-2}\,M_\odot$ of neutron rich material is expelled on dynamical (GW) timescales, i.e., within 5–10 ms after merger, and with characteristic velocities of $\sim (0.1-0.3)c$, see e.g., [2337, 3164–3168]. Two main mechanisms are responsible for these dynamical ejecta: the tidal interaction between the two merging objects [3164, 3169] and the shock developing at the collisional interface [2337, 3165, 3166, 3170]. The former is more relevant in the case of NS-BH mergers, asymmetric BNS mergers and stiff nuclear EOSs. The latter is the dominant mechanism in the case of equal mass BNSs, and leads to mass mainly being expelled at the first bounce of the two NS cores [2337]. In the case of soft nuclear EOSs, the merging NSs are more compact, the merger is more violent, while the remnant reaches higher temperatures. A small fraction of the shocked component can reach high-speeds, up to $\sim 0.8c$ [2337, 3166]; this fast-tail has a non-trivial dependence on the EOS [3171] and is relevant for the kilonova afterglow [3172]. The merger remnant can unbind a total mass of $\sim 10^{-2} M_\odot$ during its evolution on viscous timescales of $(0.1-1)$ s throughout various wind mechanisms (spiral-wave and disk winds). Binaries with short-lived NS remnants and/or with mass ratio $\gtrsim 1.4$ (including NS-BH) produce remnant BH with massive hyperaccreting disks whose evolution is dominated by viscous and thermal effects. Turbulent viscosity of magnetic origin, neutrino absorption or EM interaction with a strong, large-scale magnetic field have been proven to be very efficient in unbinding a significant fraction (between 10 and 40%) of the accretion disk resulting from the merger dynamics, see e.g. [3173–3177]. At a quantitative level, it is important to notice that the amount of ejected matter, its composition and, in the case of BNS mergers, the lifetime of the remnant are influenced by both intrinsic binary parameters, as the total mass and the mass ratio, see, e.g., [2339, 3178], and nuclear EOS-related properties,

JCAP03(2026)081